Nonlinear X-ray Absorption of Graphite

Scientific work to obtain the academic degree
Master of Science (M. Sc.)

by

Lars Hoffmann

submitted on November 7, 2019
Institute of Chemistry and Biochemistry
Department of Biology, Chemistry and Pharmacy
Freie Universität Berlin

Supervisor:	Prof. Dr. Michael Zürch
First examiner:	Prof. Dr. Eckart Rühl
Second examiner:	Prof. Dr. Martin Wolf

Abbreviations

XUV	extreme ultraviolet
MD	molecular dynamics
FEL	free-electron laser
eV	electronvolt
SASE	self-amplified spontaneous emission
Ti:Sa	titanium-sapphire
MOD	modulator
RAD	radiator
HHG	high-harmonic generation
SHG	second-harmonic generation
THG	third-harmonic generation
SFG	sum-frequency generation
DFG	difference-frequency generation
Nd:YAG	neodymium-doped yttrium aluminum garnet
PES	photoelectron spectroscopy
MO	molecular orbital
HOPG	highly oriented pyrolytic graphite
nTTM	extended two-temperature model
FWHM	full width at half maximum
PADReS	photon analysis, delivery, and reduction system
HZB	Helmholtz-Zentrum Berlin
CCD	charge-coupled device
HDF	hierarchical data format
NIST	national institute of standards and technology
DFT	density functional theory

Contents

1. Introduction

Nonlinear absorption is a phenomenon that is known for the visible light region since the 1940s.[1] After the invention of the laser it became an important factor for modern laser technologies. Nonlinear absorption occurs when the absorption changes at higher light intensity. The absorption can be increased in the case for e.g. two-photon absorption or decreased when the ground state of the electronic transition gets depleted. The latter is also called saturable absorption.[2,3] Since it requires intense light to observe the phenomenon, it is limited the wavelength regions for which lasers exist. It took decades until a suitable light source was invented to expand the nonlinear absorption into the extreme ultraviolet (XUV) and X-ray region. In 2009 for the first time nonlinear absorption was reported in the XUV.[2] With the use of the free-electron laser FLASH (Hamburg, Germany) saturable absorption was observed of the L-shell transition of aluminum with photon energies of 92 eV (13 nm). Since then it was reported for the Sn N-edge at 24 eV (52 nm) and Fe K-edge at 7.1 keV (0.17 nm).[3,4] Due to the high photon flux the ground state was depleted which made the sample transparent to the remaining X-ray pulse. The opposite case of reverse saturable absorption is known for the Al K-edge at 1560 eV (0.79 nm) and carbon K-edge at 285 eV (4.35 nm). It was inferred that the reduced transmission is due to two-photon absorption.[5,6]

The electromagnetic spectrum covers wavelengths from meters (radio waves) to picometers (γ-radiation). In between are the microwave, infrared, visible, ultraviolet and X-ray region. There are no exact boundaries for these regions. The distinction can be made by the sources of the radiation. For example γ-photons are generated by transitions in the atomic nucleus while X-rays are generated by transitions of inner-shell (core) electrons. Latter can be used in X-ray spectroscopy which is of great use, because of its element-specific property. Each inner shell transition has its own unique excitation energy which are well documented.[7] E.g. the carbon 1s-electrons have an ionization energy of 284.2 eV.

Carbon is polymorphic. There are two natural allotropes of carbon, diamond and graphite which consist of sp^3 and sp^2 hybridized atoms, respectively. In diamond the sp^3 hybridized carbon atoms form a 3d network, whereas graphite consists of 2d graphene layers which are weakly bound by van der Waals forces. Carbon has six electrons in $1s^2 2s^2 2p^2$ configuration. The 1s-electrons do not form chemical bonds. The 2s, $2p_x$ and $2p_z$ electrons form three sp^2 hybridized orbitals which overlap to σ-bonds in a plane with a 120° angle. The $2p_z$ electrons form delocalized π-orbitals. Like in aromatic molecules the C-C bond length is shorter than a C-C single bond. The delocalized π-electrons are highly mobile and are the the reason for the electric conductivity.[8,9] In 1985 the first synthetic carbon allotrope called Buckminsterfullerene named after the architect Richard Buckminster Fuller was published.[10] There exist fullerenes with the sum formula C_{60}, C_{70}, C_{76}, C_{80} and more. Fullerenes

are spherical structures consisting of rings of five or six carbon atoms. In 1991 another synthetic carbon allotrope was first created, the carbon nanotube.[11] In 2004 the graphene monolayer could be isolated[12] and lead to the development of many more exotic carbon allotropes such as the graphyne which contains sp, sp^2 and sp^3 hybridized carbon atoms.[9]
There are many useful applications for the carbon allotropes. Because of the outstanding physical properties, graphene is appealing for applications in electronics. The extraordinary fast charge-carrier transport in graphene makes it useful for transistors and integrated circuits.[13] Carbon nanotubes have been successfully applied in pharmacy and medicine. Due to their high surface area they are able to adsorb a variety of therapeutic agents (e.g. drugs, antibodies or vaccines). Further, carbon nanotubes can be used for tissue regeneration, biosensor diagnosis, enantiomer separation of chiral drugs and extraction of drugs and pollutants.[14]
While the solid state of matter of carbon is well researched, little is known about the liquid state. To produce liquid carbon extreme pressure ($\sim$ MPa) and temperature ($\sim$5000 K) are required. These conditions are almost impossible to achieve in a laboratory setting at equilibrium.[15] In geology and astrophysics these extreme conditions are present. It is likely that the liquid carbon exists in lower earth mantle.[16] It is also presumed that it is formed on Uranus and Neptune. With the use of lasers materials can be driven through non-equilibrium pathways into novel regimes of matter. One of these pathways is the process of non-thermal melting.[17,18] Focusing intense laser pulses onto a solid sample lead to strong electronic excitation and following lattice destabilization.[18] The lattice breaks and undergoes melting and ablation. Jeschke et al. simulated the melting of graphite following excitation by a femtosecond laser pulse above damage threshold.[19] The MD simulation shows that the graphite structure changes significantly in the timescale of 1 ps after excitation and the graphite reaches a liquid-like state within 1 ps.
To investigate processes the probe needs to be faster than the mechanism involved. In order to examine a process that concludes within 1 ps, hence in femtosecond timescale, a probe with less femtoseconds or even attoseconds is needed. Ultrashort laser pulses fulfill this requirement. Since the invention of lasers in 1960[20] the achievable pulse duration shortened from nanoseconds, over picoseconds and femtoseconds to attoseconds. While attoseconds pulses can be made in the X-ray region,[21] they don't have the necessary intensity to drive absorption experiments into the nonlinear region.
In today's research the most used source of high brightness X-rays is the spontaneous radiation from electrons moving in undulator magnets of an electron storage ring, so-called synchrotron radiation. It has very useful properties such as tunable wavelength, high flux, high brilliance, high stability, polarization (linear and circular) and pulsed time structure. But the pulse length has its limits at 10-100 ps.[22] A further development of the electron accelerator facilities are the free-electron lasers (FEL) which improve the properties of the synchrotron facilities by orders of magnitude. In FEL facilities pulse durations down to a few femtoseconds are possible.[23]
In this experiment the nonlinear absorption of graphite and liquid carbon is investigated. In a pump-probe setup the phase transition of graphite is studied.

2. Fundamentals

Spectroscopy is the study of the interaction between light and matter. To understand the interactions it is important to know about light itself. The questions what light is can lead to multiple answers. That are light is an electromagnetic wave and that light consists of particles called photons. Since the concept of quantum mechanics was invented we know that both answers individually can't fully describe light. It is rather a mix of both and can be explained with the concept wave-particle duality. Quantum particles can be describes by waves and light can sometimes act as a wave and sometimes as a particle. Here we start to describe light with the wave picture but also use the quantized nature of photons to explain the absorption of light in matter.

2.1 Ultrashort Laser Pulses

The basis of light as a electromagnetic wave are Maxwell's equations

$$\vec{\nabla} \times \vec{E}(\vec{r},t) = -\frac{\delta \vec{B}(\vec{r},t)}{\delta t} \tag{2.1}$$

$$\vec{\nabla} \times \vec{H}(\vec{r},t) = \frac{\delta \vec{D}(\vec{r},t)}{\delta t} + \vec{j}(\vec{r},t) \tag{2.2}$$

$$\vec{\nabla} \cdot \vec{D}(\vec{r},t) = \rho(\vec{r},t) \tag{2.3}$$

$$\vec{\nabla} \cdot \vec{B}(\vec{r},t) = 0 \ . \tag{2.4}$$

which form the foundation of classical electromagnetism and optics. In dielectric materials are no free charges and currents

$$\rho(\vec{r},t) = 0 \tag{2.5}$$

$$\vec{j}(\vec{r},t) = 0 \ . \tag{2.6}$$

There are the following relations between the electric and magnetic quantities

$$\vec{D}(\vec{r},t) = \epsilon_0 \epsilon(\vec{r}) \vec{E}(\vec{r},t) \tag{2.7}$$

$$\vec{B}(\vec{r},t) = \mu_0\mu(\vec{r})\vec{H}(\vec{r},t) \ . \tag{2.8}$$

The dielectric function ϵ and magnetic permeability μ can be set to unity in our consideration. The dielectric constant of the vacuum ϵ_0 and the magnetic permeability of the vacuum μ_0 are related connected to the speed of light in vacuum c by

$$c = \frac{1}{\sqrt{\epsilon_0\mu_0}} \ . \tag{2.9}$$

By using the equations (2.5), (2.6), (2.7) and (2.8) Maxwell's equation can be simplified to

$$\vec{\nabla} \times \vec{E}(\vec{r},t) = -\mu_0\mu\frac{\delta\vec{H}(\vec{r},t)}{\delta t} \tag{2.10}$$

$$\vec{\nabla} \times \vec{H}(\vec{r},t) = \epsilon_0\epsilon\frac{\delta\vec{E}(\vec{r},t)}{\delta t} \tag{2.11}$$

$$\vec{\nabla} \cdot [\epsilon\vec{E}(\vec{r},t)] = 0 \tag{2.12}$$

$$\vec{\nabla} \cdot [\mu\vec{H}(\vec{r},t)] = 0 \ . \tag{2.13}$$

From equations (2.9) to (2.13) one can derive the electromagnetic wave equation of light

$$\vec{\nabla} \times \vec{\nabla} \times \vec{E}(\vec{r},t) + \frac{1}{c^2}\frac{\delta\vec{E}(\vec{r},t)}{\delta t^2} = 0 \ . \tag{2.14}$$

With the use of the Laplace operator[1] and some vector analysis[2] the wave equation can be written in a more intuitive form

$$\Delta\vec{E}(\vec{r},t) - \frac{1}{c^2}\frac{\delta^2}{\delta t^2}\vec{E}(\vec{r},t) = 0 \ . \tag{2.15}$$

In its complex notation a time-harmonic wave can be written as

$$\vec{E}(\vec{r},t) = \vec{E}_0(\vec{r}) \cdot e^{i(\vec{k}\vec{r}-\omega t+\varphi)} \tag{2.16}$$

also known as the plane wave equation. Inserting notation (2.16) into (2.15) leads to the solution

$$\omega^2 = c^2\vec{k}^2 \ . \tag{2.17}$$

[1] $\Delta = \vec{\nabla}^2$

[2] $\vec{\nabla} \times (\vec{\nabla} \times \vec{a}) = \vec{\nabla}(\vec{\nabla} \cdot \vec{a}) - \vec{\nabla}^2\vec{a}$

This connection of the frequency ω, wave number $\vec{k}$ and speed of light c is called the dispersion relation and is often written in the form

$$\frac{\omega}{\vec{k}} = c \ . \tag{2.18}$$

There is an infinite number of combinations of ω and $\vec{k}$ that fulfill equation (2.15). Each pair of ω and $\vec{k}$ that is a solution to the wave equation is called a mode. The plane wave equation can therefore be written as a superposition of all modes

$$\vec{E}(\vec{r},t) = \sum_{i=1}^{\infty} \vec{E}_{0,i}(\vec{r}) e^{i(\vec{k}_i\vec{r}-\omega_i t+\varphi_i)} \ . \tag{2.19}$$

In Figure 2.1 the electric field for a single mode (a) and for 21 modes (b) is illustrated. In the first case the electric field oscillates continuously (harmonic oscillator). When multiple waves with different ω overlap, the electric fields add up and with no phase difference ($\varphi_i = 0$) it leads to a peak at t_0, because all modes add up constructively. As the result of superposition of many modes this "beating" pattern can be increased by adding more modes which leads to even shorter pulses. We now consider a optical pulse at a fixed position $\vec{r} = 0$ in space. Assuming linear polarization of the light field, we can write the real electric field strength $E(t)$ as a scalar quantity that can be described as a harmonic wave multiplied with a temporal amplitude or envelope function $A(t)$

$$E(t) = A(t) e^{i(\varphi_0-\omega_0 t)} \ . \tag{2.20}$$

The situation where the phase $\varphi_0 = 0$ is called a cosine pulse. When $\varphi_0 = -\pi/2$ and the maxima of the carrier oscillations don't match the maximum of the envelope is called a sine pulse. We can add an additional time dependent phase term $\varphi_a(t)$ to the temporal phase function of (2.20)

$$\varphi(t) = \varphi_0 + \omega_0 t + \varphi_a(t) \ . \tag{2.21}$$

The momentary light frequency $\omega(t)$ can be defined as

$$\omega(t) = \frac{\mathrm{d}\varphi(t)}{\mathrm{d}t} = \omega_0 + \frac{\mathrm{d}\varphi_a(t)}{\mathrm{d}t} \tag{2.22}$$

This additional phase term describes the variation of the frequency in time which is called a chirp. From (2.22) we can see that a quadratic time dependence of the spectral phase leads to a linear dependence in the time domain. A positive $\mathrm{d}\varphi_a(t)/\mathrm{d}t$ is called an up-chirp, a negative derivation is called a down-chirp. In Figure (2.2) a cosine pulse without chirp (a), with an up-chirp (b) and with a down-chirp (c) are displayed.
The real-valued electric field $E(t)$ of an ultrashort light pulse at a fixed point in space can be Fourier transformed into monochromatic waves

$$E(t) = \frac{1}{2\pi} \int_{-\infty}^{\infty} \tilde{E}(\omega) e^{i\omega t} \mathrm{d}\omega \ . \tag{2.23}$$

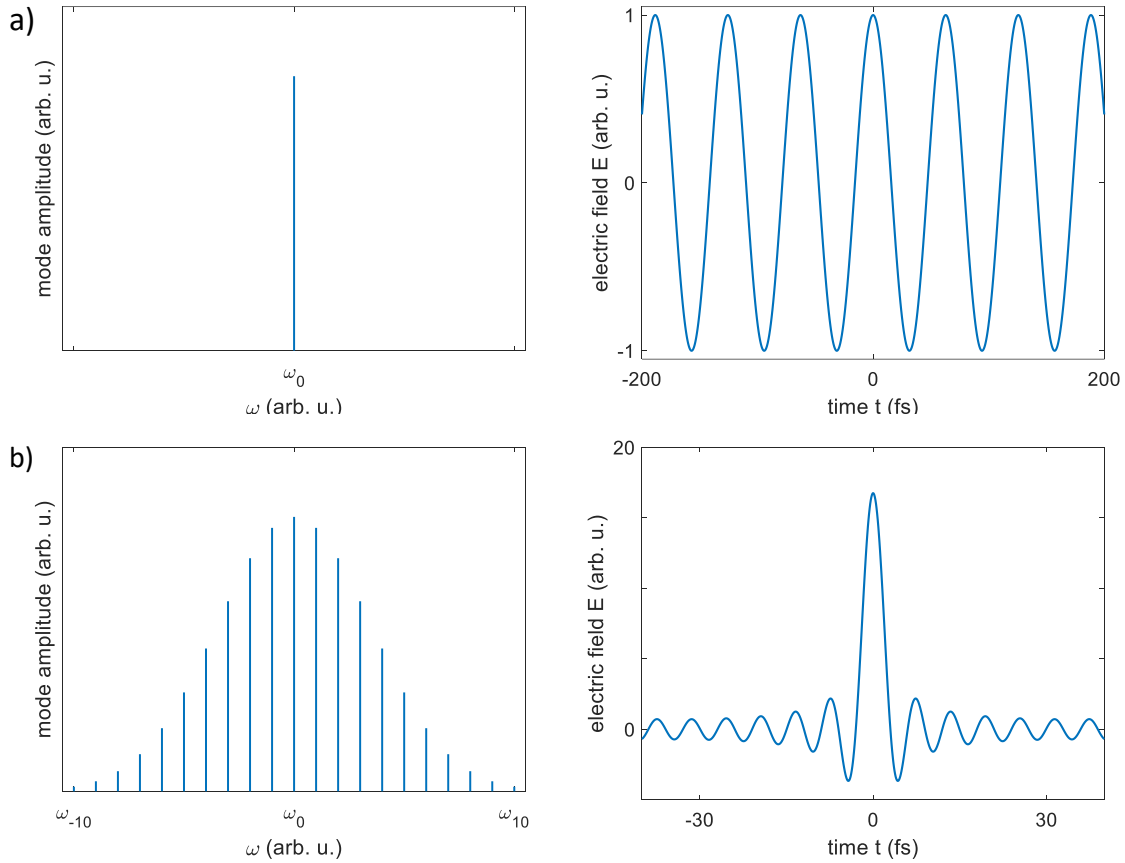

Figure 2.1: The real part of the electric field (right) for their respective modes (left). a) A single mode with frequency ω_0 leads to a electric field E oscillation continuous in time. b) Many modes ω_{-10} to ω_{10} with a Gaussian profile and no phase difference ($\varphi_i = 0$) form a pulsed electric field.

By inverse Fourier transform the spectrum $\tilde{E}(\omega)$ can be obtained

$$\tilde{E}(\omega) = \int_{-\infty}^{\infty} E(t) e^{-i\omega t} \mathrm{d}t \ . \tag{2.24}$$

The electric field $E(t)$ as a physical quantity must be real in the time domain. The Fourier transform can only lead to real values when there is the symmetry relation in the frequency domain

$$\tilde{E}(\omega) = \tilde{E}^*(-\omega) \ , \tag{2.25}$$

where $*$ denotes complex conjugation. The knowledge of the spectrum for positive frequencies is sufficient for a full description of the light field. The positive part of the spectrum can be defined as

$$\tilde{E}^+(\omega) = \tilde{E}(\omega) \quad \text{for} \quad \omega \geq 0 \quad \text{and} \tag{2.26}$$

$$0 \quad \text{for} \quad \omega < 0 \quad . \tag{2.27}$$

The amplitude $A(t)$ is given by

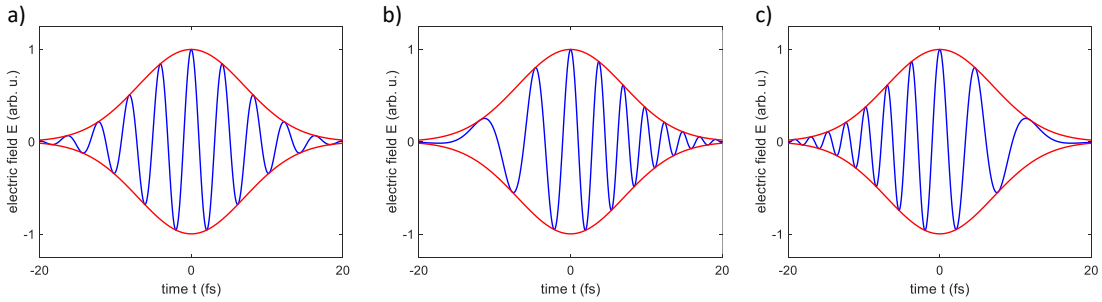

Figure 2.2: Electric field $E(t)$ (blue) with Gaussian envelope (red) for a cosine pulse a), a up-chirped pulse with positive quadratic phase b) and a down-chirped pulse with negative quadratic phase c). The parameter a was chosen to be $\pm\, 0.04\,\mathrm{fs}^{-2}$.

$$A(t) = 2|E^+(t)| = E^+(t)e^{i\varphi(t)} \quad . \tag{2.28}$$

The fundamentals of ultrashort laser pulses are part of a variety of textbooks in physics and optics. This chapter is based on the book by Träger.[24]

2.2 Free-Electron Laser

The free-electron laser (FEL) is a evolution of the synchrotron radiation facilities. Although the FEL is not a classical laser in the sense, that it has a cavity with an active medium that is pumped to population inversion, its properties which include, among other things, high monochromaticity, high power, pulsed time structure and small divergence, justify the name.[22] In a FEL electrons are accelerated in vacuum tube to relativistic speeds with energies up to 17.5 GeV.[25] The accelerated electrons traverse a periodic magnet structure, called undulator, in which the electrons oscillate and emit radiation.
The radiation of a FEL and a synchrotron are both generated by undulators. The main difference is length of the undulator which can be over 100 m in a FEL and is only a few meters in a storage ring. The wavelength λ is given by the undulation equation[26]

$$\lambda = \frac{\lambda_u}{2\gamma^2}\left(1 + \frac{K^2}{2} + \gamma^2\theta^2\right) \tag{2.29}$$

where λ_u is the undulator period, θ the radiation angle in forward direction, γ the Lorentz contraction factor

$$\gamma = \frac{1}{\sqrt{1 - \frac{v^2}{c^2}}} \tag{2.30}$$

and K the undulator parameter

$$K = \frac{eB_0\lambda_u}{2\pi mc} \tag{2.31}$$

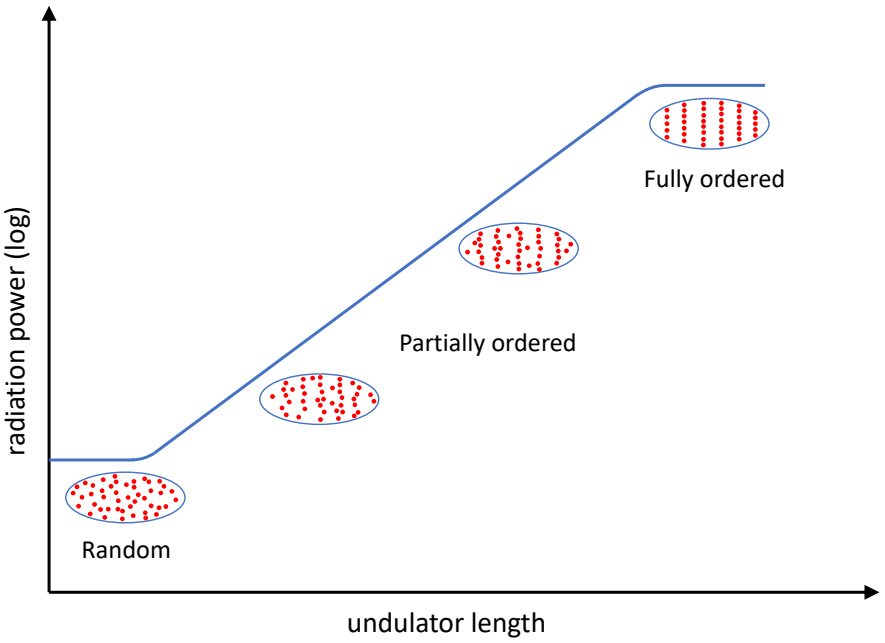

Figure 2.3: Scheme for the growth of the radiation power due to the electron beam microbunching as a function of the undulator length.

with the peak magnetic density B_0.[27] We can see from equation (2.29) and (2.30) that the wavelength gets shorter with increasing electron velocity v. In a FEL the electrons and the emitted X-rays travel together through the undulators at about the same velocity. The X-rays travel with the speed of light c, while the electrons have a slightly lower velocity

$$v = \left(1 - \frac{\sqrt{1 + \frac{K^2}{2}}}{2\gamma}\right) c \ . \tag{2.32}$$

The electrons undergo one cycle of sinusoidal motion for one period of magnet structure they traverse. The X-ray wave advance one wavelength with respect to the electrons as it propagates on the same path. This is the so called "slip condition", the electron's "slippage" one cycle (one wavelength) behind the co-propagating wave.[26] The slip condition enables constructive interference, because both electrons and wave undergo one phase cycle per magnet period. The very long undulators in FELs lead to much stronger radiated fields which enables "microbunching" of the electrons to a wave with increasing modulation. The more electrons participate in the microbunching the stronger the emitted electric field becomes which induces more electrons to participate in microbunching. This leads to a feedback driven exponential growth of electron bunching and electric fields which is the foundation of the high powers (GW) of free-electron lasers.

In Figure 2.3 the power gain curve for a X-ray FEL is displayed. In the beginning of the undulator the electron have random positions in the bunch and there no density

modulation. The motion of the relativistic electrons is defined by the Lorentz force

$$\vec{F} = \frac{\mathrm{d}\vec{p}}{\mathrm{d}t} = -e(\vec{E} + \vec{v} \times \vec{B}) \tag{2.33}$$

where $\vec{p} = \gamma m v$ is the momentum and $\vec{B}$ is the magnetic flux density. The period magnetic field of the undulator is given by

$$\vec{B} = -B_0 \sin\left(\frac{2\pi z}{\lambda_u}\right) \quad . \tag{2.34}$$

When there is no electric field the electron motion follow, to first order, a $\vec{v} \times \vec{B}$ driven oscillation with

$$v_x = \frac{Kc}{\gamma} \cos\left(\frac{2\pi z}{\lambda_u}\right) \tag{2.35}$$

where z is the direction of the electron beam and x is the perpendicular direction of oscillation. In the first few meters the generated electric fields have no significant contribution to the Lorentz force and thus have little effect on the electron motion. With increasing length of the undulator the electric field of the radiation does begin to affect the electron motion and can no longer be neglected. There is a transverse coupling of the radiated electric field E_x and the transverse velocity of the electrons v_x. This leads to an energy exchange between the electrons and the fields described by

$$\frac{\mathrm{d}E_e}{\mathrm{d}t} = \vec{v} \cdot \vec{F} \tag{2.36}$$

where $E_e = \gamma m c^2$ is the electron energy and m is the electron rest mass. Inserting the Lorentz force of (2.33) in (2.36) yields the equation

$$mc^2 \frac{\mathrm{d}\gamma}{\mathrm{d}t} = -eE_x v_x \quad . \tag{2.37}$$

The energy exchange between particles ($\mathrm{d}\gamma/\mathrm{d}t$) and fields ($E_x v_x$) depends directly on the electron's position and the phase of the wave's electric field E_x. Some electrons gain energy and some lose energy, based on their relative position to the phase of their radiated electric field. An electron that receives an energy gain and thus an acceleration travels a bit further in x direction before it returns to the z axis. Likewise, an electron that receives a deceleration arrives sooner at the z axis. The electrons develop an increased charge density at some positions and a reduced charge density at others. This charge density modulation is the reason for microbunching. The radiated electric field grows with the number of participating electrons N_e and thus the radiated power grows with N_e^2. At a certain distance in the undulator almost all electrons participate in the microbunching and are now fully ordered or fully modulated and the power growth reaches saturation.
This process is called self-amplified spontaneous emission or SASE and is used in most FEL facilities such as LCLS[28] (Stanford, USA), FLASH[29] (Hamburg, Germany) and SACLA[30] (Hyogo, Japan). The FEL facilities that operate using SASE are able to achieve high powers up to 60 GW[26] but have a limited shot-to-shot re-

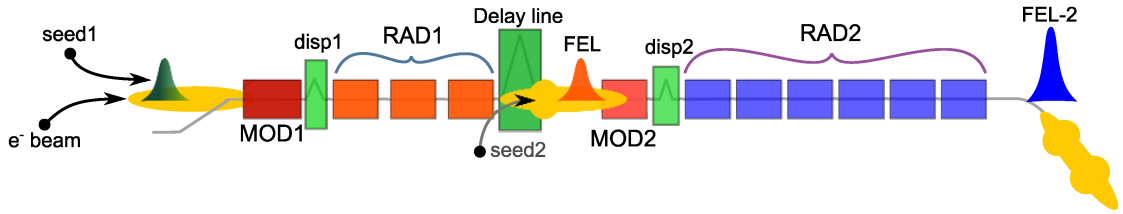

Figure 2.4: Layout of the free-electron laser at FERMI. The electron bunch and the seed pulse, i.e. the third harmonic of a Ti:Sa laser 260 nm, interact in the modulator (MOD). In the dispersive section (disp) the electron beam undergoes microbunching and in the radiator (RAD) emits coherent light at one of the seed harmonics (>20 nm). The light of the first FEL stage enters the second FEL stage where it interacts with a high harmonics seed to produce light with wavelength down to 4 nm.[33] b) Tuning curves for FERMI FEL-1 (dashed lines) and FEL-2 (solid lines) for the electron beam energies of 0.9, 1.2 and 1.5 GeV. The isolated markers represent numerical simulations.[34]

producibility and longitudinal coherence due to the statistical properties inherited in spontaneous emission process that is SASE.[31] These properties can be significantly improved by using an external seed. The FEL at FERMI (Trieste, Italy), where the experiment of this thesis was performed, is one of few facilities that employ a seeded setup instead of SASE.[32]

The layout of the undulator line of FERMI is shown in Figure 2.4. It consists of two parts. Both parts contain a modulator, a dispersive section and multiple radiators. The first part is seeded with by the third harmonic of a Ti:Sa laser at 260 nm. In the modulator, which is a relatively short undulator, the electron bunch is tuned to the seed laser's frequency. In the dispersive section the electron beam is microbunched. The radiators together form a long undulator section which is tuned to the nth harmonic of the seed wavelength λ. The emitted FEL radiation has a wavelength λ/n. The FEL light of the first section is used as a seed for the second section. A fresh electron bunch is needed for the second section. Therefore the electrons of the first section are slowed down in a delay line and an electron bunch unaffected by the first section enters the second section, where the undulators are tuned to even higher harmonics of the initial seed pulse.[35] For 4 nm radiation the 65th harmonic of the 260 nm seed laser is needed which is already the 3rd harmonic of a Ti:Sa laser. So to say the FEL can generate the 195th harmonic of the initial radiation.

2.3 Nonlinear Optics

The intense light of lasers can modify the optical properties of a material. There are many nonlinear optical phenomena, which are nonlinear in a sense that they occur when the response of a material to an applied optical field depends nonlinearly on the strength of the electric field.[36] For example the high harmonic generation (HHG) mentioned in the previous chapter is a nonlinear effect.

Let us first consider the polarization $P(t)$ of a material. In conventional (i.e. linear)

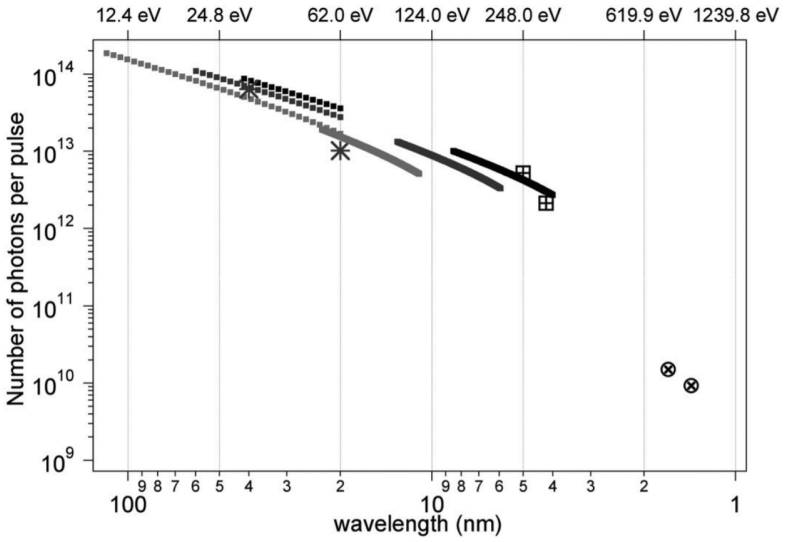

Figure 2.5: Tuning curves for FERMI FEL-1 (dashed lines) and FEL-2 (solid lines) for the electron beam energies of 0.9, 1.2 and 1.5 GeV. The isolated markers represent numerical simulations.[34]

optics the induced polarization depends linearly on the electric field strength

$$P(t) = \epsilon_0 \chi^{(1)} E(t) \ , \tag{2.38}$$

where ϵ_0 is the permittivity in vacuum and $\chi^{(1)}$ is the linear susceptibility. With intense light sources this is not the case. The equation (2.38) can be rewrittten by expressing $P(t)$ as a power series in electric field strength $E(t)$

$$P(t) = \epsilon_0 \left[\chi^{(1)} E(t) + \chi^{(2)} E^2(t) + \chi^{(3)} E^3(t) + ... \right] \ , \tag{2.39}$$

where $\chi^{(2)}$ and $\chi^{(3)}$ are the second- and third-order nonlinear optical susceptibilities, respectively.[3] If we assume a monochromatic electric field $E(t) = E_0 e^{-i\omega t}$ similar to equation (2.16) and a medium with non vanishing $\chi^{(2)}$ we obtain the polarization

$$P = \epsilon_0 \left[\chi^{(1)} E_0 e^{-i\omega t} + \chi^{(2)} E_0^2 e^{-i2\omega t} + \chi^{(3)} E_0^3 e^{-i3\omega t} \right] \ . \tag{2.40}$$

It contains a term with doubled frequency 2ω and a term with tripled frequency 3ω. This is the basis for the so called second-harmonic generation (SHG) and third harmonic generation (THG). The efficiency of SHG and THG depends on the relative size of $\chi^{(1)}$, $\chi^{(2)}$ and $\chi^{(3)}$ which are material properties. To get a rough overview of the orders of magnitude we can make an estimate. If the nonlinearity is electronic in origin, one can expect the lowest order correction term $P^{(2)} = \chi^{(2)} E^2(t)$ to be comparable to a linear response $P^{(1)} = \chi^{(1)} E(t)$ when the electric field strength is of the order of the characteristic atomic field strength[36]

$$E_{at} = \frac{e}{4\pi\epsilon_0 a_0^2} \ , \tag{2.41}$$

[3]For simplicity the electric field $E(t)$ and polarization $P(t)$ are treated as scalar quantities.

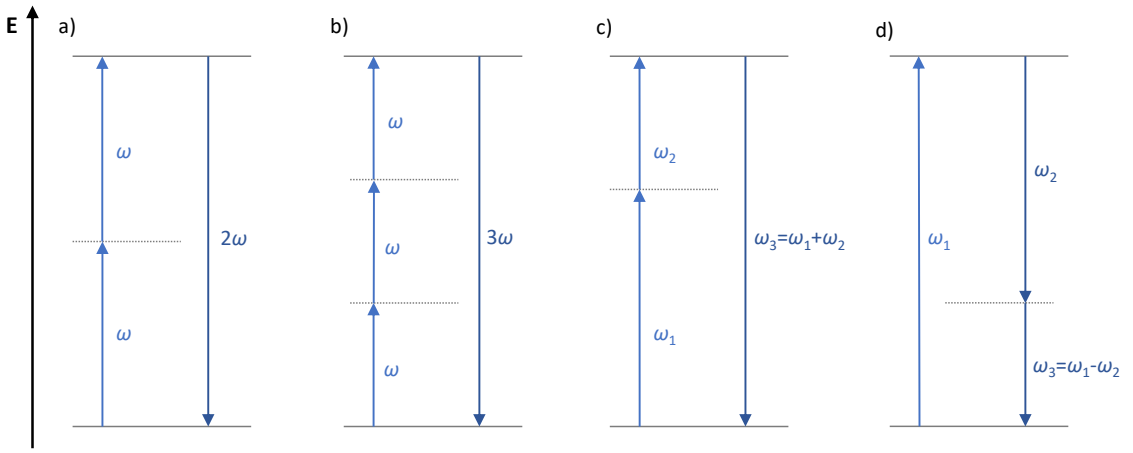

Figure 2.6: Energy diagrams for different nonlinear effects. a) second-harmonic generation (SHG), b) third-harmonic generation (THG), c) sum-frequency generation (SFG) and difference-frequency generation (DFG).

where a_0 is the Bohr radius of the hydrogen atom

$$a_0 = \frac{4\pi\epsilon_0\hbar^2}{me^2} \quad . \tag{2.42}$$

We find that $E_{at} = 5.14 \cdot 10^{11}\,\mathrm{V/m}$. Under the condition of nonresonant excitation we expect $\chi^{(2)}$ to be of the order of $\chi^{(1)}/E_{at}$. With $\chi^{(1)}$ being of the order of unity we expect $\chi^{(2)}$ to be

$$\chi^{(2)} = \frac{1}{E_{at}} \approx 2 \cdot 10^{-12}\,\frac{\mathrm{m}}{\mathrm{V}} \quad . \tag{2.43}$$

Likewise, one expects $\chi^{(3)}$ to be of the order of $\chi^{(1)}/E_{at}^2$ which yields

$$\chi^{(3)} = \frac{1}{E_{at}} \approx 4 \cdot 10^{-24}\,\frac{\mathrm{m}^2}{\mathrm{V}^2} \quad . \tag{2.44}$$

Again, this is only an estimation and for certain cases, e.g. resonant excitation, the nonlinear susceptibilities can be greatly increased.[37] Also, the nonlinearities scale with $E^n(t)$, so they become more relevant for higher intensities.

In Figure 2.6 the energy diagrams of the above mentioned second-harmonic generation (SHG) and third-harmonic generation (THG) are shown. In SHG two photons with the same frequency generate a single photon with double the frequency. In THG three photons with the same frequency generate a single photon with triple the frequency. In sum-frequency generation (SFG) two photons with different frequency generate a photon with the sum of their frequency and in difference-frequency generation (DFG) two photons with different frequency generate a photon with the difference of their frequency. All four nonlinear phenomena can only happen when light interacts with matter. They are parametric processes which means they satisfy energy and momentum conservation. For SFG that means

$$\hbar\omega_1 + \hbar\omega_2 = \hbar\omega_3 \quad \text{and} \tag{2.45}$$

$$\hbar\vec{k}_1 + \hbar\vec{k}_2 = \hbar\vec{k}_3 \ . \tag{2.46}$$

Equation (2.46) is also known as the phase matching criteria.[38] Only when the waves are in phase it is possible to achieve constructive interference and a macroscopic signal output. The phase mismatch $\Delta\vec{k}$ defines a coherence length

$$l_{\text{coh}} = \frac{1}{\Delta\vec{k}} \ . \tag{2.47}$$

If the sum-frequency is generated in the bulk, the medium has to be shorter than the coherent length. In practice that means that l_{coh} has to be at least a few millimeters long which demands a corresponding low phase mismatch $\Delta\vec{k}$.
A method to reach the XUV and soft X-ray region is the high harmonic generation (HHG). In the previous chapter it was mentioned as a seed source for the second FEL stage at FERMI. Here a short description is given. HHG is a highly nonlinear effect that occurs when gas atoms are exposed to strong laser fields. It was first reported in 1989 when Li et al. observed the 33rd harmonic of a Nd:YAG laser.[39] Experimentally, high harmonics are generated by focusing a laser into a vacuum chamber containing a small gas target. Often noble gases are used. The larger noble gases like Xenon or Krypton have better conversion efficiencies while the smaller gases like Helium and Neon generate shorter wavelengths. The generated harmonic spectra usually consist of a perturbative region, a plateau with nearly constant conversion efficiency and an abrupt cutoff. The cutoff position was found to follow the universal law $I_P + 3.17U_P$, where I_P is the ionization potential and U_P is the ponderomotive potential

$$U_P = \frac{e^2E^2}{4\pi\omega^2} \ , \tag{2.48}$$

which is the mean kinetic energy acquired by an electron oscillating in the laser field.[40]

In Figure 2.7 the three step model of high-harmonic generation is shown. In a strong laser field the Coulomb potential becomes distorted and the potential barrier is lowered. An electron is set free by tunnel ionization. The electron is accelerated away from the nucleus and gains kinetic energy. The laser field changes its sign and the electron is accelerated towards to nucleus. It recombinates with the ion and emits a photon. The photons energy is determined by the kinetic energy of the electron. The time the electron is set free with respect to the laser field is important. The electron could be emitted too early and gains too much energy to move back and recombinate with the core when the field changes its sign. When the electron is emitted late there isn't much time to accelerate before recombination occurs. The emission time is the reason for the many different high-harmonics that are generated in this process and it explains the sudden cutoff in the high-harmonics spectra.[24]

2.4 Basic Absorption Processes

Radiation can interact with matter in many different ways. Here we want to review the basic absorption and emission processes that are important in the X-ray region.

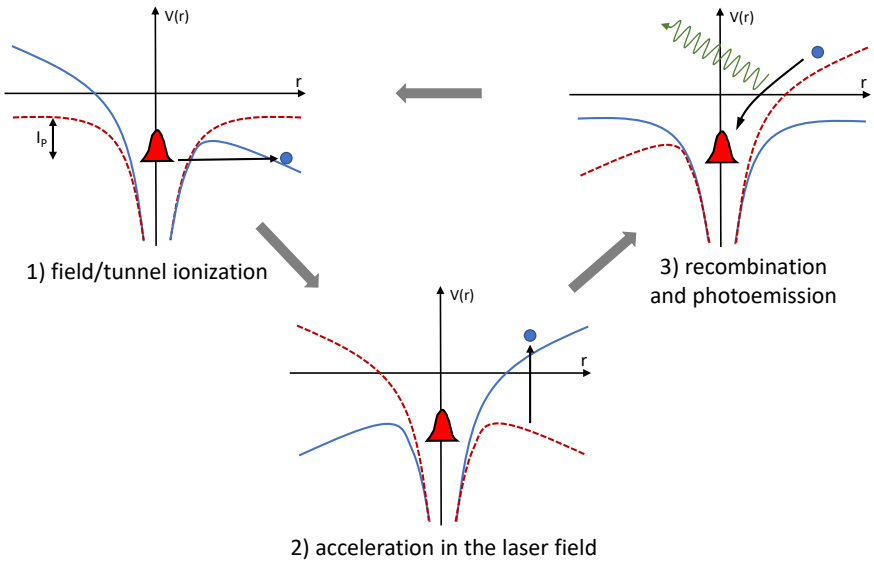

Figure 2.7: The three-step model of high-harmonic generation: 1) the laser field distorts the Coulomb potential and lowers the barrier for an electron to be set free by tunnel ionization, 2) the electron is accelerated in the laser field, 3) the laser field changes its sign and causes the electron to move back to the core and recombinate by emitting the high-harmonic photon.

In Figure 2.8 simplified models of the atom are shown. The electrons orbit around the nucleus with a positive charge $+Ze$. The electron orbits are labeled in the X-ray notation K, L, and M and correspond to the principal quantum numbers $n = 1, 2, \text{and} 3$, respectively. The other quantum numbers are neglected in this model. Because of their high photon energy, X-rays typically excite the low-lying core electrons. Shown in Figure 2.8a) is the ionization of an atom by an electron. The primary electron with sufficient kinetic energy E_p is scattered while knocking a K electron (secondary electron) out of the atom. The scattered electron has the reduced kinetic energy E'_p, because the transferred energy is used to overcome the binding energy and supply kinetic energy of the secondary electron E_s. The electron collision induced ionization leaves a core vacancy which can be filled by higher-lying electrons in either a radiative or non-radiative process which is shown in c) and d). In b) the photoionization process is shown. An incident X-ray photon with sufficient energy is absorbed by a core electron, which is then ionized. The emitted photoelectron has a kinetic energy

$$E = h\nu - E_B \ , \tag{2.49}$$

where E_B is the binding energy of the electron. Equation (2.49) is also the foundation for the photoelectron spectroscopy (PES) where the kinetic energy of the photoelectrons is measured to obtain chemical information about the material.
In both ionization processes a) and b) the ion is left with a core vacancy. This state is not stable and the ion rearranges itself for minimum total energy by filling the vacancy with an electron from a higher shell. The excess energy that stems from this readjustment can released in two competing processes. In c) the ion releases the excess energy by emitted a photon. This process is called fluorescence. In d) the energy is released by emitting a second electron, the so called Auger electron.

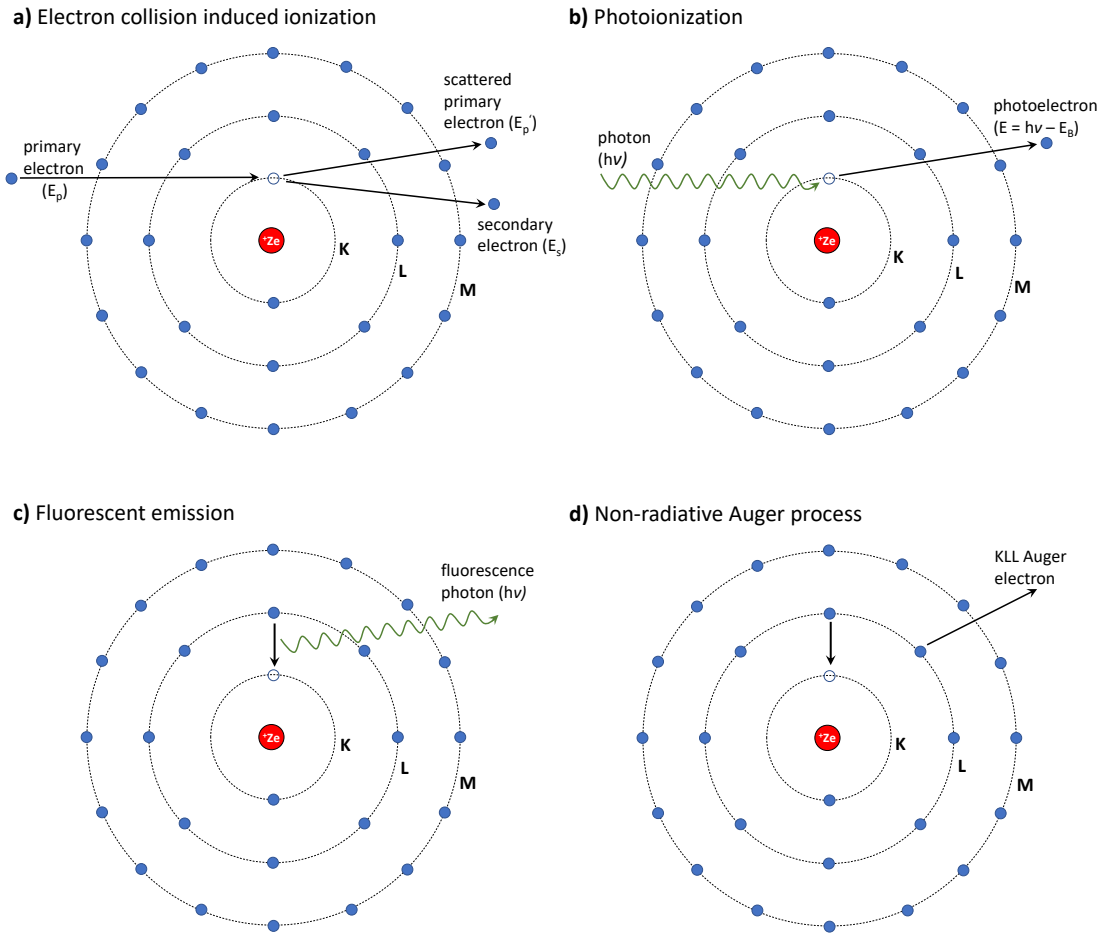

Figure 2.8: Basic absorption and emission processes in the X-ray region using a simplified atomic shell model. a) An incident primary electron with sufficiently high energy E_p knocks free a core electron and is scattered in the process. The primary electron travels in a new direction with reduced energy E_p'. The lost kinetic energy is transferred to the secondary electron and is used to overcome the binding energy. b) An incident X-ray photon $h\nu$ is absorbed by a K-shell electron which is then ionized. The kinetic energy is the difference of the photon energy and the binding energy of the electron. c) An electron with a core vacancy readjusts by filling the vacancy with a higher-lying electron. The excess energy is given away by emission of photon with characteristic energy (fluorescence). d) An atom with a core vacancy readjusts by filling the core vacancy with a higher-lying electron. The excess energy is given away by emitting a second electron (Auger electron). This electron can be from the same shell or higher depending on the energy to be released.

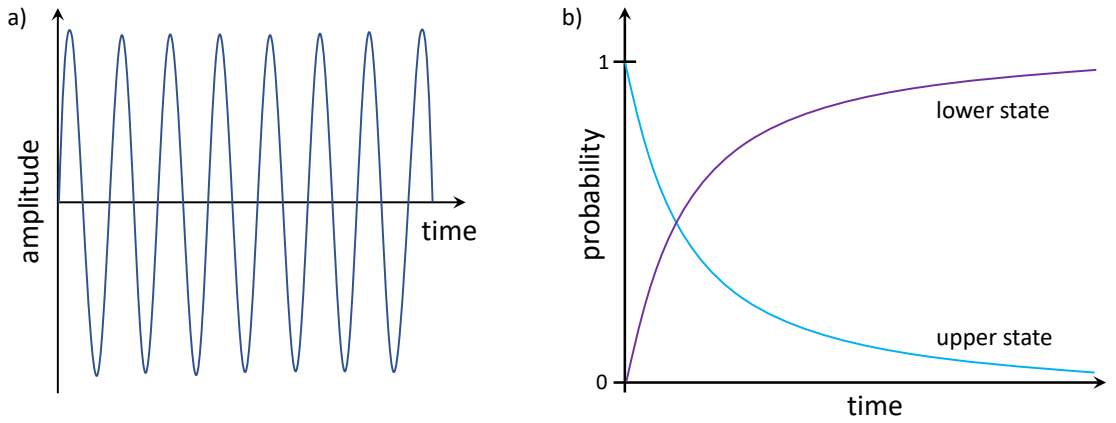

Figure 2.9: Radiative decay from an upper state Ψ_i to a lower state Ψ_f. a) The mixed states oscillates between the two states at frequency ω_{if}. b) The probability of finding the atom in the upper state decays to zero, while the probability of the lower state increases to unity.

The electron can be from the same shell as the electron that filled the vacancy or from a higher shell, depending on the energy difference of the involved shells. The nomenclature for the Auger process shown in d) is KLL, K for the vacancy, L for the electron that fills the vacancy and again L for the emitted Auger electron. When the electron that fills the vacancy aswell as the Auger electron do not come from the valence shell, the ion still has vacancies and needs further radiative or not non-radiative readjustments. The Auger effect occurs with higher probability in low Z elements while the fluorescence favors high Z elements.[41]
Not every X-ray absorption has to lead to ionization. There can be electron excitations to bound or virtual states. The excited state has a limited lifetime. During the transition from the higher energy state Ψ_i (initial) to the lower energy state Ψ_f (final) the average position of the electron oscillates between the two states at a frequency equal to the difference in energies

$$\omega_{if} = \frac{(E_i - E_f)}{\hbar} \quad . \tag{2.50}$$

Quantum mechanically the atom is in a mixed state in which the the probability of finding the atom in the upper state gradually diminishes while the probability of finding it in the lower state increases.[26]
In the presence of intense laser fields it is possible to ionize with photon energies lower than the ionization energy. Different mechanisms can be distinguished. There are the multiphoton ionization, the tunnel ionization, the field ionization and above-threshold ionization. The multiphoton ionization is a process in which multiple photons are absorbed to overcome the ionization barrier. The previously mentioned second-harmonic and third-harmonic generation (Figure 2.6) are similar mechanisms. In the tunnel ionization the laser field distorts the Coulomb potential so that the potential barrier is lowered and electrons are able to tunnel through the barrier. This process was also explained in three-step model of high-harmonic generation. The field ionization is very similar to the tunnel ionization. The difference is that the laser field lowers the potential that much that some energetic states lie above the potential barrier. The above-threshold ionization is a process in which

more photons are absorbed than energetically required for ionization.

2.5 Graphite and Liquid Carbon

Graphite is the thermodynamically stable phase of carbon at standard conditions. The structure consists of planar layers of condensed rings of six carbon atoms. A single layer is called graphene analogously to condensed aromatic compounds like anthracene. Within the layers the atoms are connected by σ- and π-bonds. The different graphene layers are kept together by van der Waals forces. Every carbon atom is surrounded by three nearest neighbors in the form of an equilateral triangle. The valence orbitals $2s$, $2p_x$ and $2p_y$ are sp^2 hybridized and form three σ-bonds with an angle of 120°. The fourth electron is in the $2p_z$ orbital perpendicular to the layer. The p_z orbitals of neighboring carbon atoms overlap and form π-bonds. They form molecular orbitals that extend over the whole layer. Every ring has formally two π-bonds, but in fact all CC-bonds are equal. The bond length of 141.5 pm is a bit longer than in benzene (140 pm).[42] The atoms at the edge of the graphite are highly reactive and usually saturated with -H or -OH groups.
The most common graphite form (Figure 2.10) crystallizes in a hexagonal structure with the space group $P6_3/mmc$ (no. 194). It has the lattice parameters a $a = 246$ pm and $c = 671$ pm. The graphene layers are stacked ABABAB. The dark color and the high conductivity within a graphene layer are attributed to the π-electrons which are delocalized over the entire graphene layer in a two-dimensional electron gas. The overlap of the π-orbitals results in a valence band (binding MO) and a conduction band (antibinding MO). The bands overlap slightly which leads to metal-like conductivity. Perpendicular to the layers the electric conductivity is 10^5 times smaller than in parallel orientation. The individual layers are 335 pm apart. The van der Waals forces which hold them together are much weaker than the covalent bonds within the graphene. This makes graphite easy to be cleaved parallel to the hexagonal plane.
There are natural occurences of graphite and it is mined in order of tonnage in China, Canada, Brazil and Madagascar.[42] Graphite is also synthetically produced. The highly oriented pyrolytic graphite (HOPG) is a pure form of synthetic graphite which is used for the this experiment.[43,44]
While the solid phase of carbon is well researched, little is known about the liquid phase of carbon. In the phase diagram after Bundy et al.[46] (Figure 2.12) we can see that extreme pressures (>10 MPa) and temperatures (>5000 K) are required to produce the liquid state. These conditions are impossible to achieve in a laboratory at equilibrium and this state cannot be isolated. With the use of lasers this it is possible to achieve this state transiently by the process of non-thermal melting.[17,18] By exciting a significant portion of the electrons into the π^*-orbital the bonds get weakened and are able to break. The resulting fluid material has the properties analogous to those of the liquid. The liquid remains at the initial material density for a time in the order of picoseconds due to inertial confinement before ablation occurs. With an ultrafast technique the liquid carbon can be probed. In this way liquid carbon could be produced from many different carbon allotropes e.g. graphite, diamond, fullerenes and amorphous carbon.[47]
The phase transition got investigated using ab-initio molecular dynamics.[48][49] It was found that the liquid carbon has two-, three-, and fourfold coordinated atoms,

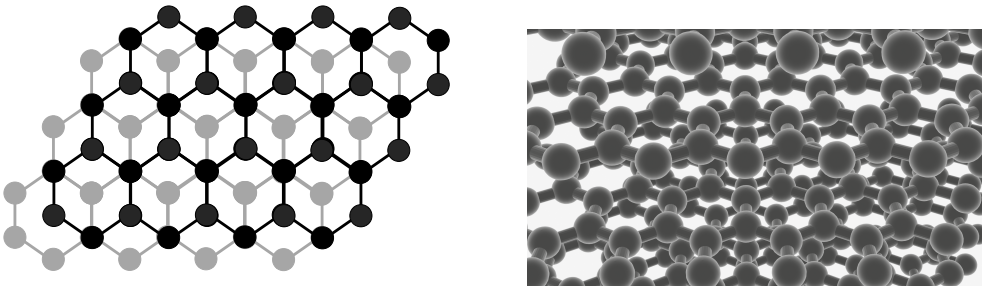

Figure 2.10: Crystal structure of the hexagonal graphite (left) with a 3d render (right). Hexagonal graphite has the space group $P6_3/mmc$ (no. 194) with the lattice parameters $a = 246\,\text{pm}$ and $c = 671\,\text{pm}$. The graphene layers are stacked ABABAB. In the left picture the layer A is shown in black and layer B is shown in gray. Half of the carbon atoms don't have a next neighbor in the adjacent layer.[45]

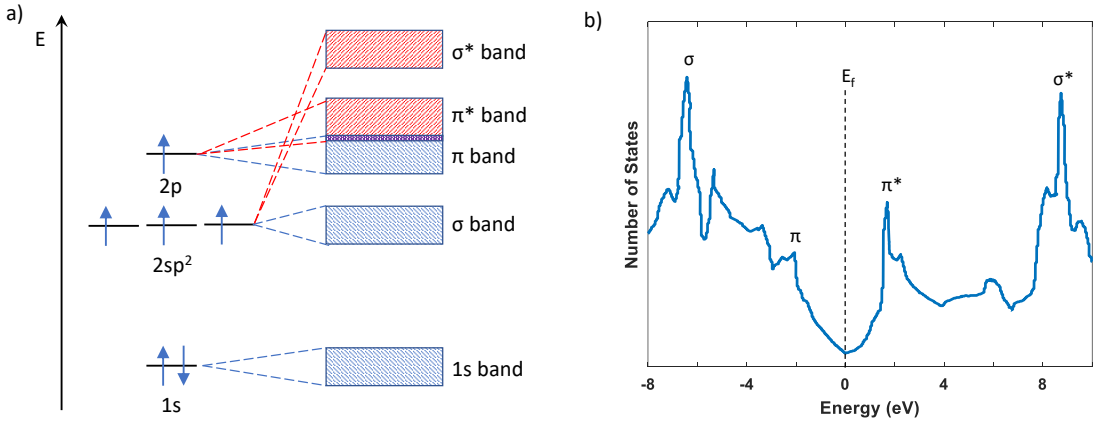

Figure 2.11: Bonding in graphite. a) MO diagram for the the sp^2 hybridized carbon and the resulting band structure in graphite.[50] b) Joint density of states of graphite calculated with density functional theory by Ooi et al.[51] The small overlap of the valence band (π) and the conduction band (π^*) is the reason for the electric conductivity in graphite.

while half of them are threefold. The biggest change occurs in the region from 2500-3000 K where *sp*-bonded carbon chains are formed. At 5000 K is average coordination number was found to be 2.9 and ring structures with 7-8 atoms were calculated. The liquid state has the conductivity of a metal, because of the merging of the π- and π^*- orbitals. Because the π-bonds are weaker they are expected to be broken first, before the σ-bonds are cleaved.

The electrons transfer their energy to the lattice by electron-phonon coupling. By using an extended Two-Temperature Model (nTTM) of Mincigrucci et al.[52] we can get a better understanding of that process in liquid carbon. A nTTM simulation is based on a set of coupled rate equations and permits to calculate the density of the conduction electrons induced by a pump pulse, as well as the temperatures of the electron and lattice subsystems (Figure 2.13). The electron density is increased through absorption of an intense laser pulse ($\lambda = 400\,\text{nm}$, 100 fs FWHM) and has a peak at $4.3 \cdot 10^{22}\,\text{cm}^{-3}$, then rapidly decreases in a few picoseconds to value of $10^{-21}\,\text{cm}^{-3}$ primarily due to Auger recombination. The electron temperature reaches 4 eV ($\approx 10^4$ K). There is no direct coupling of the between the pump pulse and the

lattice. The energy transfer is due to the electron-phonon coupling, which equalizes both temperatures at $T \approx 0.8\,\mathrm{eV}$ within half a picoseconds. The electron-phonon coupling was set to $\tau_{EP} = 10\,\mathrm{fs}$ in agreement to the literature.[53]
The nTTM allows us to get an idea of the time it takes for the graphite to melt. This quantity is important to know when performing a pump probe experiment for studying liquid carbon.

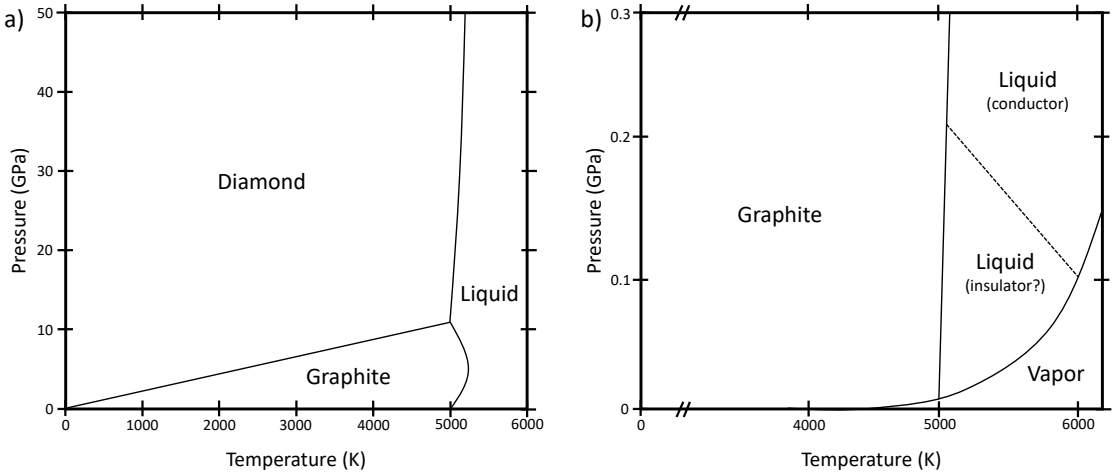

Figure 2.12: Phase diagram of carbon after Bundy et al.[46] with different pressure scales in a) and b). Graphite is the thermodynamically stable phase of carbon at standard conditions. Diamond exist at high pressures with temperatures up to 5000 K. At temperatures beyond 5000 K exists the gas phase at low pressure and the liquid phase at higher pressure.

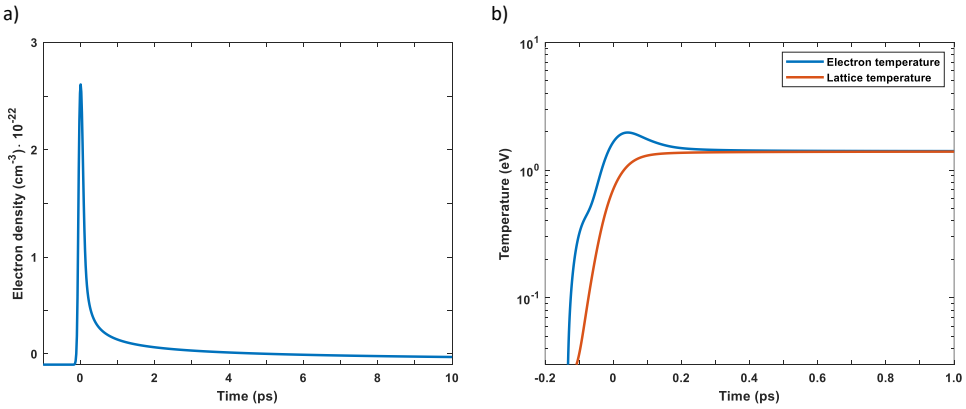

Figure 2.13: Properties of graphite excited by an intense laser pulse calculated by an extended Two-Temperature Model (nTTM) by Mincigrucci et al.[52] a) The density of free electrons is increased drastically at excitation and decays within picoseconds primarily due to Auger recombination. b) Mean temperature of the electrons and the lattice. The energy is transferred to the lattice by electron-phonon coupling. The coupling time was set to $\tau_{EP} = 10\,\mathrm{fs}$ in agreement to the literature.[53] Within half a picosecond the electron and lattice temperature have equalized at $T \approx 0.8\,\mathrm{eV}$.

3. Experimental Part

3.1 Experimental Design

This experiment was performed at EIS-TIMEX beamline of the FERMI free-electron laser at the Elettra synchrotron light source in Trieste, Italy. The experimental setup is shown in Figure 3.1. The FERMI FEL-2 is based on a double high gain high harmonic generation (HGHG) conversion where the first FEL stage serves as a pump for the second stage (see Section 2.2). The FEL propagated through the Photon Analysis, Delivery, and Reduction System (PADReS) that includes shot-to-shot photon diagnostics, e.g. I_0 monitor. Also the drain current from the ellipsoidal mirror functioned as an additional I_0 monitor. Three different FEL photon energies of 261.6 eV (4.74 nm), 285.7 eV (4.34 nm), and 309.2 eV (4.01 nm) with a pulse duration of 25 fs (FWHM) were used. The FEL beam was focused on a 12×12 μm^2 spot size and spatially overlapped the optical beam in collinear orientation. The optical beam was produced by a Ti:sapphire laser upconverted to the second harmonic (wavelength $\lambda = 400$ nm, pulse duration $\tau = 100$ fs FWHM, spot size $60 \times 60\,\mu m^2$). The FEL was tuned to maximum pulse energy, which was fluctuating between 4 - 28 µJ for each shot (see appendix Figure 6.1). The optical pulse energy was set to 5 µJ, 8 µJ or 30 µJ.
The samples were highly oriented pyrolytic graphite (HOPG) films from Lebow Inc. with different thickness of 80 nm, 100 nm, and 200 nm. The samples were mounted on a xyz-stage inside a vacuum chamber (pressure $p \approx 1 \cdot 10^{-7}$ mbar). The transmitted X-ray beam was dispersed by a grating (HZB 1603-2, 1000 gr/mm) onto a CCD camera (Andor iKon-M SO).
The optical laser was synchronized to the FEL. By using the same seed for both optical laser and FEL a jitter of less than 10 fs could be achieved which aside of the high coherence of the seeded FEL radiation are special characteristics of the FERMI FEL rendering it suitable for nonlinear optical experiments.[54] The optical pulse was used as a pump and the FEL pulse a probe. By changing the time delay between these two the samples could be investigated at different times after the pump. The samples were raster scanned to get the most number of shots per graphite film. A single pump-probe pulse pair burned a hole into the graphite film (see Appendix Figure 6.2). The focus of the FEL and optical beam had to be readjusted each shot in regards to the folds of the graphite film.

3.2 Data Analysis

Datasets were collected for various combinations of FEL wavelength, film thickness, optical pulse energy and time delay. Each dataset consists of 50 - 471 shots (most of

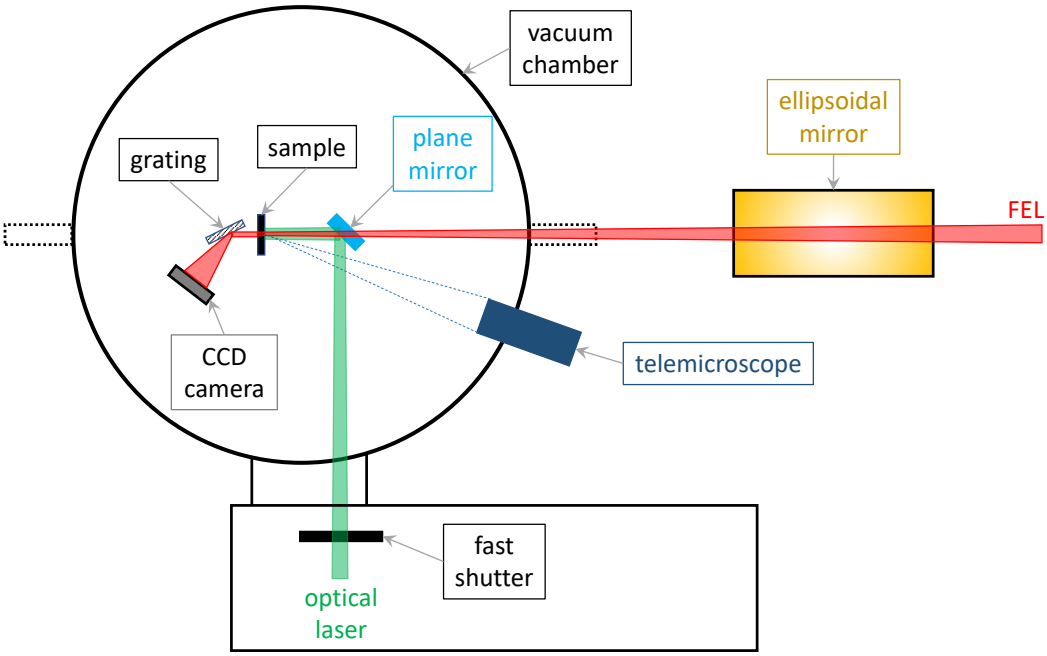

Figure 3.1: Experimental setup at the EIX-TIMEX beamline at FERMI. The FEL pulse (wavelength $\lambda = 4.01 - 4.74\,\text{nm}$, time duration FWHM $\approx 25\,\text{fs}$, pulse energy $E_P = 4 - 18\,\mu\text{J}$) were focused on a $12 \times 12\ \mu\text{m}^2$ spot size and spatially overlapped with the optical beam in collinear orientation. The latter was a Ti:sapphire laser upconverted to the second harmonic (wavelength $\lambda = 400\,\text{nm}$, pulse duration $\tau = 100\,\text{fs}$ FWHM, pulse energy $E_P = 5 - 30\,\mu\text{J}$, spot size $60 \times 60\ \mu\text{m}^2$). The samples were highly oriented pyrolytic graphite (HOPG) films (80 nm, 100 nm, and 200 nm thick) from Lebow company. The samples were mounted on a xyz-stage inside a vacuum chamber (pressure $1 \cdot 10^{-7}\,\text{mbar}$). The transmitted beam was dispersed by a grating (HZB 1603-2, 1000 gr/mm) onto a CCD camera (Andor iKon-M SO).

them have >200 shots). The data was saved in HDF files containing a multitude of information about the FEL beam diagnostics, optical laser and instruments inside the vacuum chamber. The data analysis was performed in MATLAB.[55]
For data analysis the FEL X-ray intensity before target interaction I_0 is important. I_0 was measured by PADReS and also by the ellipsoidal mirror. Because there was no filter in front of the detector at PADReS, the measurement included undesired photons of the first FEL stage. Though, they were filtered out before entering the experimental chamber. The I_0 measurement by the ellipsoidal mirror didn't include the undesired photons but had no energy calibration beyond being proportional to the intensity. To get to know the extent of the uncertainties at the I_0 measurement by PADReS, the shot-to-shot measurements by both detectors are plotted against each other (see Appendix Figure 6.3). By extrapolating the data an error of about $0.5\,\mu\text{J}$ of the I_0 measured by PADReS was determined.
The CCD camera was positioned in a way that the fundamental of the FEL is not displayed to avoid saturation. The stray light on the CCD image (see Appendix Figure 6.4), which is due to grating imperfections, is integrated and used as a measure for the transmitted X-rays. The transmitted X-ray intensity is plotted against the FEL intensity (Figure 3.2). By taking advantage of the FEL intensity fluctuations,

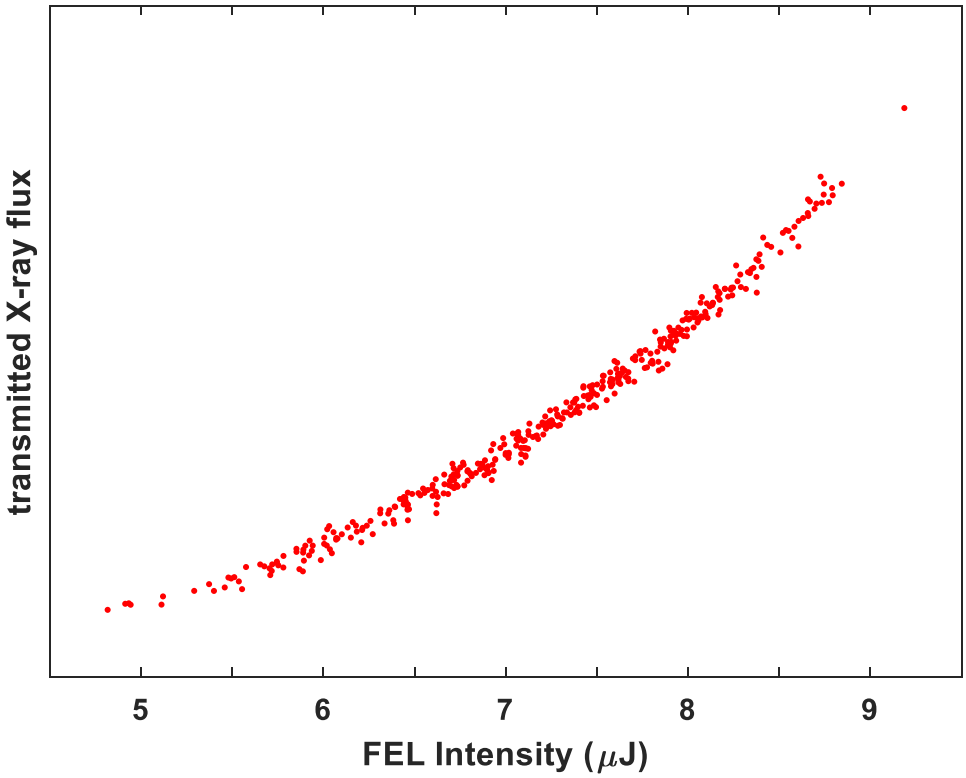

Figure 3.2: Experimental data for the transmitted X-ray flux vs FEL intensity. Dataset for wavelength 309.2 eV, 80 nm film, 5 µJ optical laser and time delay −1 ps. Each point represents one FEL pulse.

data could be collected for intensities in the range of 4-28 µJ. By applying the fit function

$$\mathrm{f}(I_0) = g + bI_0 e^{-(\alpha_\mathrm{L} + \alpha_\mathrm{NL} I_0)d} \tag{3.1}$$

the absorption coefficients were extracted. I_0 is the initial X-ray intensity, α_L and α_NL are the linear and nonlinear absorption coefficients, d is the sample thickness, b and g are parameters that are needed, because only a fraction of the transmitted light is measured. More information on the use of this fit function is given in the next chapter.

Table 3.1: Overview of the measured time delays with their respective photon energy, sample thickness, laser energy and number of shots taken. Negative time delays mean that the FEL hits the sample first.

	261.6 eV	285.7 eV	309.2 eV
time delay (ps)	sample thickness (nm) | laser energy (μJ) | # shots		
1.15	100 | 30 | 152		
1.00		80 | 8 | 372	80 | 5 | 399
0.15	100 | 30 | 199		
0.10	100 | 30 | 418		
0.05		80 | 8 | 471	80 | 5 | 374
0.00	200 | 30 | 398	80 | 8 | 465	80 | 5 | 443
−0.05		80 | 8 | 373	80 | 5 | 323
−0.08		80 | 8 | 246	
−0.10		80 | 8 | 453	
−0.12		80 | 8 | 161	
−0.15		80 | 8 | 186	
−0.25		80 | 8 | 267	
−0.40			80 | 5 | 87
−1.00	200 | 30 | 226		

4. Results and Discussion

The absorption of light by a homogeneous material is described by the Beer-Lambert law

$$I = I_0 e^{-\alpha d} \ , \tag{4.1}$$

where I is the transmitted light intensity, I_0 is the initial light intensity, d is the thickness of the material and α is the absorption coefficient in the dimension $[\text{length}]^{-1}$. In the case where the thickness is kept constant and only I_0 is changed, like it's done in this experiment, one would expect a linear relation between I and I_0. Provided, the absorption coefficient α is indeed a constant for a certain wavelength.
In this experiment three different wavelengths were used. They were selected to be below the absorption K-edge of carbon (261.6 eV or 4.74 nm), at the edge in resonance to the π^*-band (285.7 eV or 4.34 nm), and above the edge (309.2 eV or 4.01 nm). The X-ray absorption spectrum of graphite and the indicated wavelength are displayed in Figure 4.1.
By plotting the transmitted X-ray intensity against the incoming intensity while keeping or other parameters constant it is possible to investigate the linearity of the X-ray absorption in graphite. The plots for each wavelength are shown in Figure 4.2. The three graphs are from the datasets at time overlap ($\Delta t = 0$), because this time delay is measured for all three wavelengths and thus, enables the best comparison. The optical laser energies, however, are different. The energy is 30 µJ for 261.6 eV, 8 µJ for 285.7 eV and 5 µJ for 309.2 eV. But the 400 nm light is not transmitted and there isn't much time for the system to change drastically at time overlap. By just looking at the graphs one can see the absorption is nonlinear. At least this is the case for the two non-resonant excitations. On the edge at 285.7 eV the data points scatter more and from a qualitative view they don't show a big difference between a linear and nonlinear fit. Also the different photon energies have to be noted. The FEL was tuned to achieve the highest pulse energy. The higher the photon energies the lower the intensity the FEL could produce. Below the edge the X-ray intensity went up to 28 µJ, at the edge the highest output was at 11 µJ and above the edge the FEL could only yield up to 9 µJ. For the intense X-rays the Beer-Lambert law fails to describe the absorption correctly. Strictly speaking the Beer-Lambert law only holds true for dilute solutions and and incident flux that doesn't influence the atoms or molecules, which is definitely not the case in this experiment. To quantify the nonlinear absorption a different ansatz is needed. A possible ansatz is that the absorption coefficient α is a function of the FEL intensity I_0:

$$\alpha(I_0) = \alpha_{\text{L}} + \alpha_{\text{NL}} I_0 \ . \tag{4.2}$$

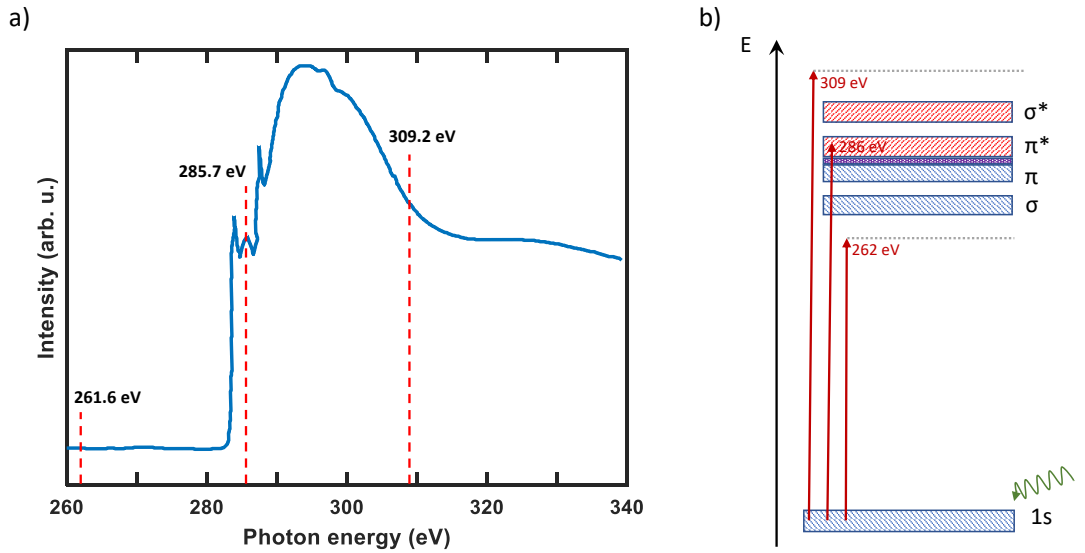

Figure 4.1: a) The X-ray absorption spectrum measured by Lam et al.[56] with the three different photon energies indicated. One of the wavelengths lies below the absorption K-edge of carbon, one is at the edge in resonance to the π^*-band and the third one lies above the edge. b) Sketch of the excitation scheme. The 1s electrons are excited into virtual states in the cases of 262 eV and 309 eV or excited in resonance to the π^*-band at 286 eV.

Here the absorption coefficient α is divided into two absorption coefficients, α_{L} the linear absorption coefficient and α_{NL} the nonlinear absorption coefficient which scales with the intensity I_0. In the literature this absorption model was used to describe the nonlinear absorption of intense ultrafast optical pulses by MoS_2 sheets.[57] By inserting Equation (4.2) into the Beer-Lambert law (4.1) a new absorption equation is obtained:

$$I = I_0 e^{-(\alpha_{\mathrm{L}} + \alpha_{\mathrm{NL}} I_0) d} \quad . \tag{4.3}$$

To be able to fit the data two more parameters have to be added. Because only a fraction of the transmitted light is measured, the parameter b is added (see Equation (3.1)). There was also a filter (Ni-50 or Pd-100) between the sample and the CCD which reduces the transmitted light for a certain amount and is reason for the parameter g. The obtained equation (3.1) is the one that is used to fit the data. The result is shown in Figure 4.2 as the blue curves. The created fit function works very well on the experimental data. At lower intensities it is similar to the linear curve and also at higher intensities it is able to describe every dataset.
Nonlinear absorption of x-rays was first reported by Nagler et al. in 2009.[2] They targeted Al foils (53 nm thick) with radiation of 92 eV (13.5 nm) above the L-edge and observed saturated absorption. The reported x-ray intensities (0.3 - 200 $\mathrm{Jcm^{-2}}$) exceeded the ones used in this experiment (0.03 - 0.20 $\mathrm{Jcm^{-2}}$). Higher intensities could be obtained, because of the use of a different FEL (FLASH) and tighter focus. Nagler et al. explained their results that the ground state gets depleted, because the relaxation time of the excited electrons is higher than the pulse duration. With intensities up to 200 $\mathrm{Jcm^{-2}}$ there are more photons in the FEL pulse than L-shell electrons in the cylindrical volume of the Al foil that is in the focus of the x-ray

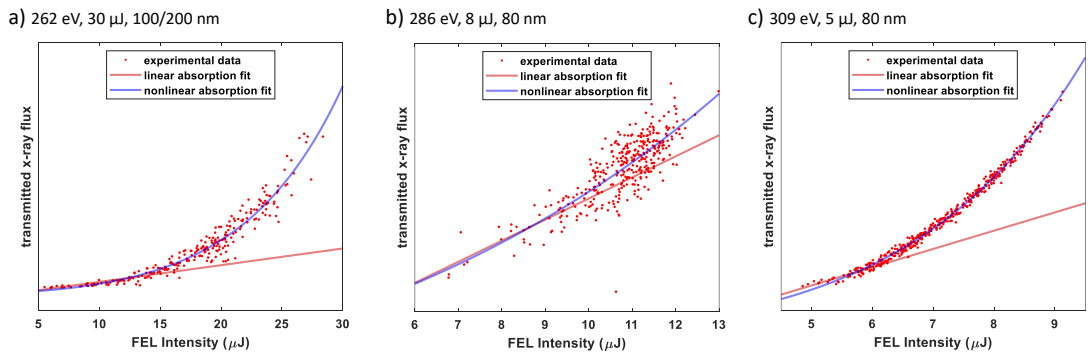

Figure 4.2: The transmitted X-ray flux against the FEL X-ray intensity before target interaction for the three different photon energies a) 262 eV, b) 286 eV and c) 309 eV. Each dot represents an FEL pulse. The blue curve is the nonlinear absorption fit. The red is a linear fit for the lower intensities which helps to see the nonlinearity of the absorption. All datasets are at time overlap ($\Delta t = 0$) but with different optical laser energies and sample thickness for each wavelength (see Table 3.1).

beam. Simply, if the relaxation time is higher than the pulse duration, not every photon can be absorbed. For our experiment the number of 1s electrons in the cylindrical volume of the beam focus exceed the number of photons per pulse by twenty times. Though, the effect is still enough to observe nonlinear absorption. After the groundbreaking work in 2009 similar experiments were done. In 2014 the nonlinear absorption of hard x-rays (7.1 keV) in iron was reported.[3] The intensities were very high (up to $9.6 \cdot 10^{19}\,\mathrm{Wcm}^{-2}$), which resulted in saturable absorption, even though the foils were much thicker (20 µm) the electron-hole lifetime were much shorter. The stronger an electron is bound the shorter is the resulting electron-hole lifetime. For the aluminum L-edge the lifetime was calculated to be 40 fs.[58] For iron the experiment suggests a lifetime of the K-hole of 500 as.[3] The K-hole lifetime was of graphite was calculated to be 7 fs.[59] The lifetime is similar to the pulse duration of the FEL (25 fs). Therefore, a high sensitivity is expected.
In a recent article[6] a similar absorption experiment for graphite at the same FEL and beamline was described. The transmission for three photon energies below, at and above the carbon K-edge was measured. They reported a reduced transmission for the resonant excitation which was ascribed to two-photon absorption. In the experiment of this thesis the opposite effect was observed. The transmission is increased which is due to the depletion of the 1s-orbital.
By using the function (3.1) not only can the experimental data be fitted, but also the absorption coefficients α_L and α_NL can be obtained. The values for the two absorption coefficients at time overlap ($\Delta t = 0$) are shown in Table 4.1. The linear absorption coefficient wavelength dependent and is compared to the literature data in Figure 4.3. The experimental result is displayed in red, literature values from NIST[60] in blue and Xraylib[61] in cyan. The absorption coefficient decreases with increasing photon energy. The experimental values follow the trend line of the NIST data, which are only available down to 1 keV, and also matches the calculated values from Xraylib at 309.9 eV and 285.7 eV. It is surprising that the value of α_L at 261.6 eV doesn't match the literature value. The experimental value doesn't decrease below the absorption edge in contrast to the literature value.
The main advantage of this experiment over the other published nonlinear absorp-

Table 4.1: Linear and nonlinear absorption coefficients α_{L} and α_{NL} for the three different photon energies at time overlap ($\Delta t = 0$). The errors are 1σ confidence intervals

photon energy (eV)	α_{L} (cm^{-1})	α_{NL} ($\mathrm{cm}^{-1}\mu\mathrm{J}^{-1}$)
261.6	$(1.24 \pm 0.01) \cdot 10^5$	$(-5.01 \pm 0.07) \cdot 10^3$
285.7	$(1.02 \pm 0.02) \cdot 10^5$	$(-1.8 \pm 0.2) \cdot 10^3$
309.2	$(1.00 \pm 0.03) \cdot 10^5$	$(-3.24 \pm 0.08) \cdot 10^4$

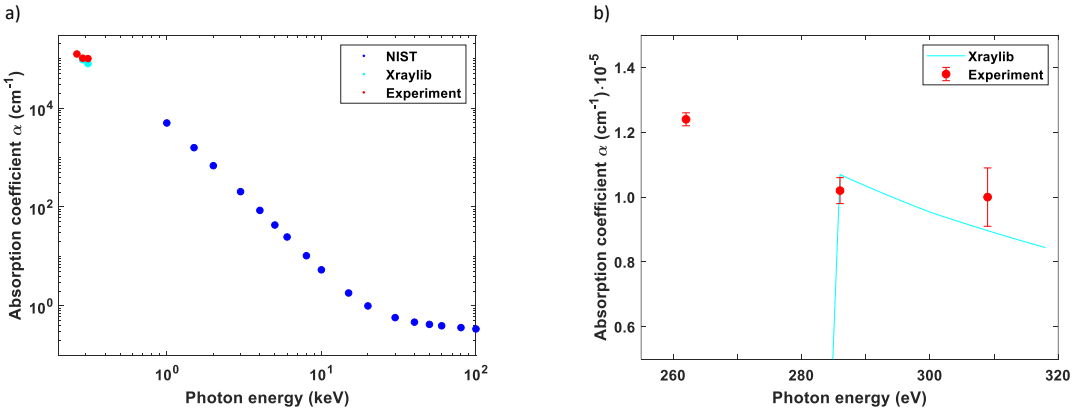

Figure 4.3: Photon energy dependence of the absorption coefficient α for graphite. The experimental result for α_{L} is displayed in red. In comparison literature values are shown from NIST[60] in blue and from Xraylib[61] in cyan.

tion experiments is the tunable time delay between the optical laser (pump) and the FEL (probe). This allows to investigate the sample at different states. Time delays from $-1.15\,\mathrm{ps}$ to $1.0\,\mathrm{ps}$ were measured. Negative values mean that the FEL hits the sample first and positive mean that the laser hits the sample first. In Figure 4.4 are the linear absorption coefficients shown in dependence of the time delay. α_{L} is shown for 261.6 eV in orange diamonds, for 285.7 eV in red squares and for 309.2 eV in dark red circles. The vertical error bars are 1σ confidence intervals and the horizontal error bars are due to the duration of the optical pulse (100 fs) which is the longer one of the two pulses. Results that are closer than 100 fs apart are averaged. Again, it is shown that higher photon energies result in lower absorption coefficients. Also, α_{L} is constant across all time delays.

The nonlinear absorption coefficients α_{NL} in dependence of the time delay are shown in Figure 4.5 for the three photon energies 261.6 eV (light blue diamonds), 285.7 eV (blue squares) and 309.2 eV (dark blue circles). The highest (absolute) nonlinear absorption coefficients are found for 309.2 eV followed by 261.6 eV. At 285.7 eV α_{NL} is the lowest of the three photon energies, which is not surprising, considering the scattered data points and the slope in Figure 4.2b. The reason for that, however, isn't clear. Perhaps, the probability of absorption is higher for the resonant transition into the π^*-band and that is the reason why more X-ray photons are absorbed, the transmission decreases and thus, α_{NL} becomes smaller. For 261.6 eV and 309.2 eV there are no real states the 1s-electrons can be excited to and the probability of absorption decreases. Also, for 285.7 eV α_{NL} decreases at $\Delta t = 0$ which could be due to the optical laser exciting valence electrons into the π^*-band

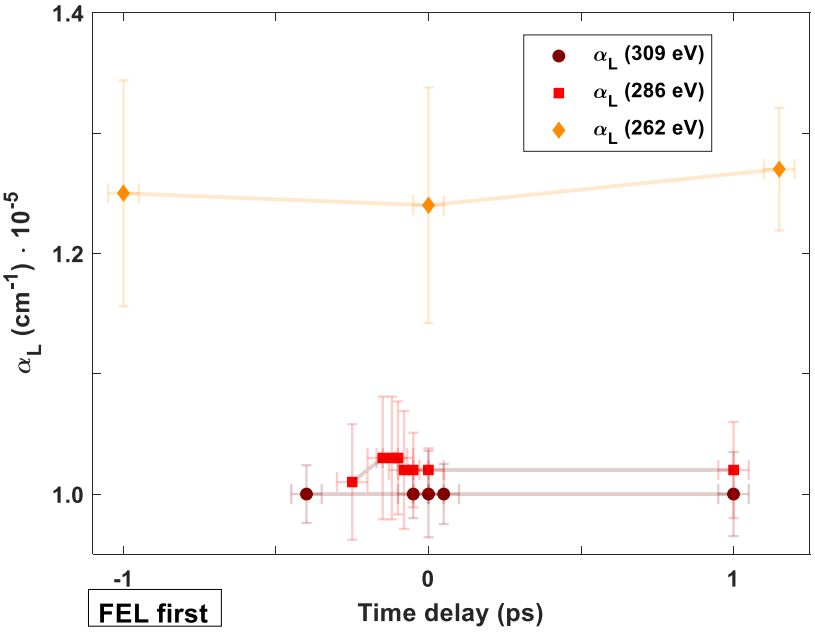

Figure 4.4: The linear absorption coefficient α_L in dependence of the time delay Δt for the three photon energies 262 eV (orange diamonds)), 286 eV (red squares) and 309 eV (dark red circles). Higher photon energies result in lower α_L in accordance to the trend in Figure 4.3. The linear absorption coefficients are constant across all time delays.

Table 4.2: Different pump energies used for the three different FEL photon energies

FEL photon energy (eV)	Laser energy (µJ)	Fluence (photons/cm^2)	eV/atom
261.6	30	$1.7 \cdot 10^{18}$	3.7
285.7	8	$4.5 \cdot 10^{17}$	1.0
309.2	5	$2.8 \cdot 10^{17}$	0.6

and thus, lowering the probability of 1s-electrons to be excited into π^*-band. It is shown that α_{NL} is different before and after the pump pulse. This is the case for all three curves. Certainly, the graphite sample undergoes significant change within 1 ps after the pump.

The sudden change in α_{NL} can be understood by comparing it a molecular dynamics simulation about the melting of graphite after excitation by an ultrafast intense laser pulse (Figure 4.6).[19] In the simulation graphite consisting of twelve graphene layers is targeted by a 20 fs laser that transfers energy of 4.0 eV/atom. These conditions are similar to our experiment (τ = 100 fs, 0.6 - 3.7 eV/atom). It shows that the graphite structure is broken apart in the first 100 fs. The boundary at which a liquid state is formed is not defined, but it can be said for sure that it happens within 1 ps. This explains the sudden change in α_{NL} at the time overlap, because the structural change happens already within the duration of the optical pulse. The value of α_{NL} at $\Delta t \approx -1$ ps doesn't change much compared to the adjacent value around $\Delta t = -10$ fs (atleast for 285.7 eV and 309.2 eV), which means that the structure change is almost completed when the pump pulse is over. The behavior of α_{NL}

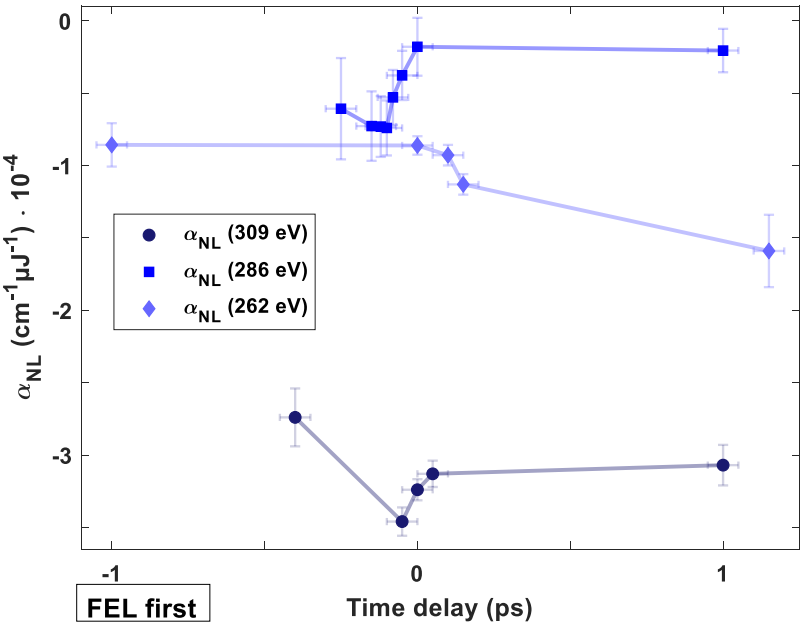

Figure 4.5: The nonlinear absorption coefficients α_{NL} in dependence of the time delay Δt for the three photon energies 262 eV (light blue diamonds), 286 eV (blue squares) and 309 eV (dark blue circles). α_{NL} is negative for all photon energies and time delays, which confirms that the graphite becomes more transmissive at higher photon energies. The highest (absolute) nonlinear absorption coefficients are found for 309 eV, followed by 262 eV and the lowest are found for 286 eV. In contrast to α_{L} does α_{NL} change significantly with the time delay.

at 261.6 eV differs from the other two photon energies. For these measurements the pulse energy was 30 µJ instead of 5 µJ or 8 µJ (see Table 4.2). The stronger pump pulse of factor ∼4 - 6 is most likely the reason for the different result. The threshold for the destruction for graphite of 3.3 eV/atom[19] is only surpassed by the 30 µJ pulse (3.7 eV/atom). Here the optical laser is able to initiate a phase transformation to liquid carbon similar to Figure 4.6). This is why the curve for 261.6 eV is different of the other two curves. Here the nonlinear absorption coefficient increases. If the value of α_{NL} at $\Delta t = -1.15$ ps can be attributed to liquid carbon, it can be stated that liquid carbon becomes more transparent at higher X-ray intensities than graphite. Additional insights can be gained by expanding the time delay range towards several picoseconds in future experiments. A measurement at every 0.1 ps would be beneficial to get a better idea of the structural change and the related absorption behavior of graphite and liquid carbon.

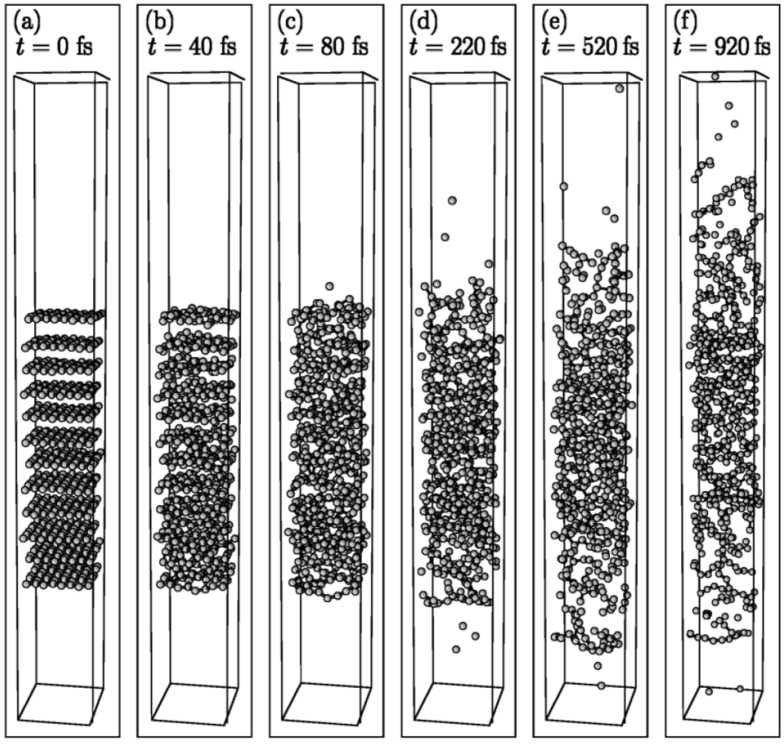

Figure 4.6: Molecular dynamics simulation for the melting of graphite by an ultrafast ($\tau = 20\,\text{fs}$) laser pulse with an energy of 4.0 eV/atom published by Jeschke et al.[19] This simulation is very similar to the experiment ($\tau = 100\,\text{fs}$, 3.7 eV/atom). It shows that the graphite structure is broken apart in the first 100 fs after excitation and liquid-like state is formed.

5. Summary and Outlook

In this thesis the absorption of intense x-rays by graphite and liquid carbon was investigated. The experiment was performed at the EIS-TIMEX beamline of the free-electron laser FERMI (Trieste, Italy). The use of an FEL enabled to probe the sample with high-intense (up to 28 µJ) ultrashort (25 fs) x-ray pulses of three different photon energies 261.6 eV (4.74 nm), 285.7 eV (4.34 nm) and 309.2 eV (4.01 nm). The energies were set to be below, at or above the carbon K-edge. The samples were thin films of highly oriented pyrolytic graphite with thicknesses of 80 nm, 100 nm and 200 nm. The FEL pulse (spot size $12 \times 12\,\mu\text{m}$) was spatially overlapped with an optical laser (wavelength 400 nm, duration 100 fs, spot size $60 \times 60\,\mu\text{m}$). Due to precise synchronization with the FEL pulse, the time delay between the two pulses could be varied. The optical pulse served as a pump pulse to induce melting of the graphite films. The transmitted x-ray light from the probe pulse was measured with a CCD camera.
The comparison of incoming and outgoing x-rays showed a nonlinear correlation with increased transmission. Using a fit equation derived from Beer-Lambert law the experimental data could be quantitatively analyzed and the linear and nonlinear absorption coefficients α_L and α_NL could be extracted. The linear absorption coefficient α_L was found to be

$$\begin{aligned}
\alpha_\text{L} &= (1.24 \pm 0.03) \cdot 10^5\,\text{cm}^{-1} \quad \text{for} \quad 261.6\,\text{eV} \\
\alpha_\text{L} &= (1.02 \pm 0.02) \cdot 10^5\,\text{cm}^{-1} \quad \text{for} \quad 285.7\,\text{eV} \\
\alpha_\text{L} &= (1.00 \pm 0.01) \cdot 10^5\,\text{cm}^{-1} \quad \text{for} \quad 309.2\,\text{eV}\ .
\end{aligned}$$

The results could be compared to the literature values for the absorption coefficient α. They follow the trend line of the literature data by NIST[60] and match the values by Xraylib for 309.2 eV and 285.7 eV.[61] Time delays were varied in the range of $\Delta t = -1.15$ ps to $\Delta t = 1.00$ ps and the dependency of α_L from the time delay was investigated. It was found that α_L is constant over all time delay.
For the nonlinear absorption coefficient α_NL a significant dependence on the time delays was revealed. At time overlap ($\Delta t = 0$) the values

$$\begin{aligned}
\alpha_\text{NL} &= (-5.01 \pm 0.07) \cdot 10^3\,\text{cm}^{-1}\mu\text{J}^{-1} \quad \text{for} \quad 261.6\,\text{eV} \\
\alpha_\text{NL} &= (-1.8 \pm 0.2) \cdot 10^3\,\text{cm}^{-1}\mu\text{J}^{-1} \quad \text{for} \quad 285.7\,\text{eV} \\
\alpha_\text{NL} &= (-3.24 \pm 0.08) \cdot 10^4\,\text{cm}^{-1}\mu\text{J}^{-1} \quad \text{for} \quad 309.2\,\text{eV}
\end{aligned}$$

were found. The negative sign indicates the reduced absorption and thereby higher transmission. α_NL changes near time overlap, because the optical pump changes the absorption behavior. At 261.6 eV the laser was exceeding the damage-threshold

of graphite, which resulted in a different time delay dependence of α_{NL}. Here, the graphite underwent a phase transition from solid to liquid carbon. The observed timescale for the phase transition matches the theoretical predictions in the literature. The linear absorption coefficient isn't sensitive to the melting. This implies that the density of the liquid is similar to the solid graphite. When the number of atoms in the focal volume doesn't change, linear absorption stays the same. However, the nonlinear absorption shows a strong dependence on the time delay. The reason for nonlinear behavior is the depletion of the 1s-orbital which is associated with the lifetime of the 1s vacancy. The lifetime of the 1s hole depends primarily on the Auger rate. In the case of instantaneous reoccupation of the 1s-orbital there would be no nonlinear absorption. In the case of the infinite lifetimes the nonlinearity would reach its maximum. For graphite the lifetime of the 1s hole was calculated to be 7 fs.[59] The change of α_{NL} can be explained with a change of the lifetime during and after the phase transition.
To get further insight the group of Tod Pascal (UC San Diego) is investigating the nonlinear response of graphite from first-principles density functional theory (DFT). In the ongoing calculations the formalism of Sharma[62] is implemented which is within independent particle approximation and time independent DFT. With this approach it is possible to calculate the second-order susceptibility $\chi^{(2)}$. Another method to evaluate $\chi^{(2)}$ is the one used by Schultze et al.[63] Here, time-dependent DFT is used to simulate the response of the desired system when perturbed by a pulse of different intensity. The theory investigations will help to find the reason for the nonlinear behavior and expand our understanding of the solid-liquid phase transition of graphite.
This experiment was not initially designed to measure nonlinear absorption. Because of that, the experimental setup could be improved for future work. It would be beneficial to leave out the grating, because there is no need for a spectral decomposition of the x-rays. Also the filter is a hindrance, because it attenuates the beam after transmission through the sample and contaminates the measurement with another absorbing material. The CCD could be replaced with a diode that is able to measure all transmitted light. Also, a systematic measurement at every 50 fs time delay, for example, as well as measuring several picoseconds after the pump could help to get a better idea about phase transition from graphite to liquid carbon.
This experiment could show the nonlinear absorption for carbon in the x-ray region which was, until now, only observed for a couple of elements. The good agreement of the measured linear absorption coefficient α_{L} with the literature shows that this setup is able to yield the right results. Here it was possible to observe the nonlinear absorption with time resolution. This opens up new experimental ways to non-equilibrium dynamics at phase transitions. The use of X-rays has the advantage of being element-selective. This can be used to investigate the phase transitions of specific elements in composite materials. The possibility of studying phase transitions helps to build diagrams. The boundaries in the phase diagrams are often not known exactly. Even in the relatively simple system such as carbon, the debate for a insulating liquid phase, for example, is going on for decades. Experiments like this contribute to the understanding of phase diagrams.

6. Appendix

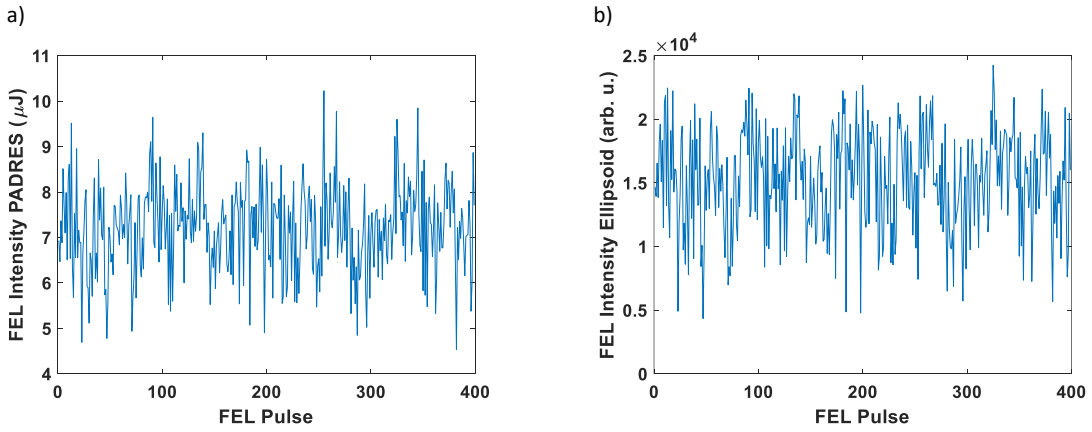

Figure 6.1: Example of the shot-to-shot pulse energy fluctuation of the FEL beam at 309.2 eV. The graphs show the two I_0 monitors a) PADReS and b) ellipsoidal mirror.

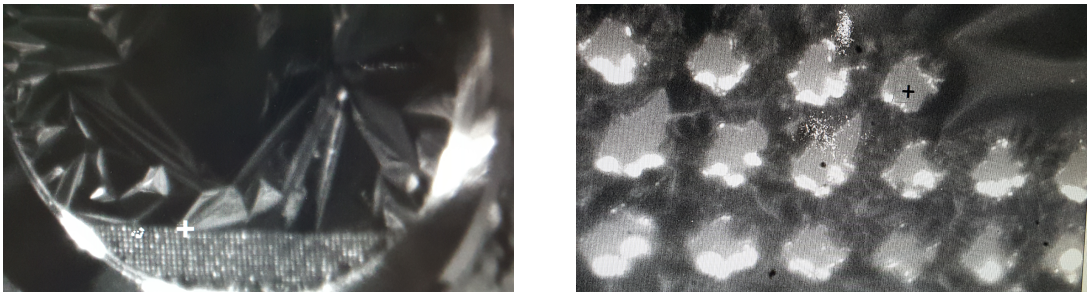

(a) (b)

Figure 6.2: Photos of the graphite films inside the chamber taken by the telemicroscope. A single pump-probe pulse pair burned a hole into the sample. The graphite film can be seen in (a) with the hole pattern on the bottom, a bigger view is shown in (b). The focus of the FEL and optical beam had to be readjusted each shot in regards to the folds of the graphite film that are visible in (a).

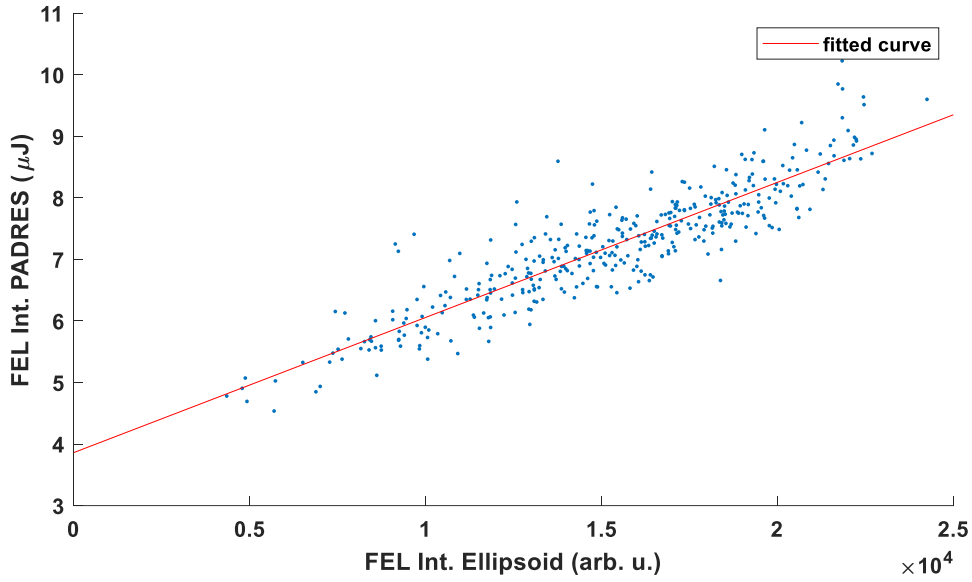

Figure 6.3: Shot-to-shot comparison of both I_0 measurements by PADReS and ellipsoidal mirror from figure 6.1. Impurities in the measurement by PADReS due to first stage FEL photons makes the it differ from the measurement at the ellipsoidal mirror. By extrapolating the data an error of about 0.5 µJ of the initial x-ray intensity was determined.

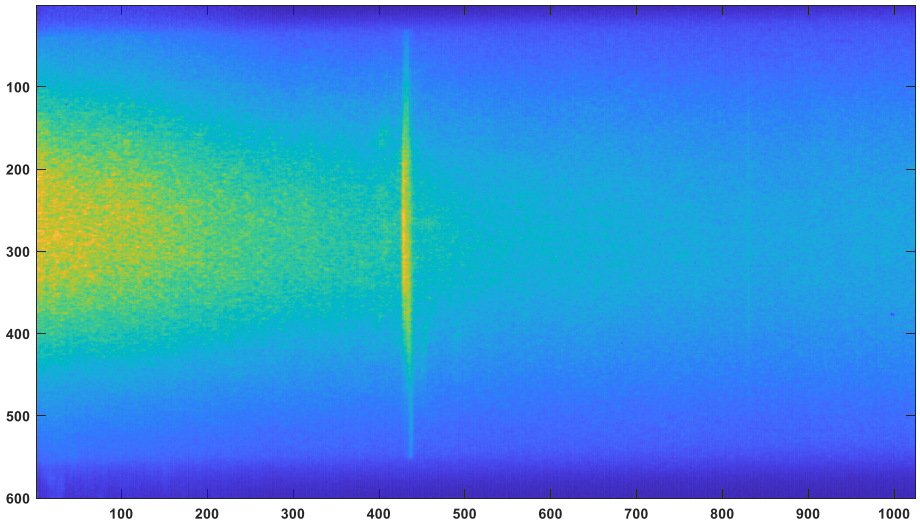

Figure 6.4: Image of the CCD camera (Andor iKON-M SO) for 309.2 eV and 80 nm film. The fundamental of the FEL is not displayed. The stray light on the left, which is due to grating imperfections, is integrated and used as a measure for the transmitted x-rays.

References

[1] G. N. Lewis, D. Lipkin, T. T. Magel, *Journal of the American Chemical Society* **1941**, *63*, 3005–3018.

[2] B. Nagler, U. Zastrau, R. R. Fäustlin, S. M. Vinko, T. Whitcher, A. J. Nelson, R. Sobierajski, J. Krzywinski, J. Chalupsky, E. Abreu, S. Bajt, T. Bornath, T. Burian, H. Chapman, J. Cihelka, T. Döppner, S. Düsterer, T. Dzelzainis, M. Fajardo, E. Förster, C. Fortmann, E. Galtier, S. H. Glenzer, S. Göde, G. Gregori, V. Hajkova, P. Heimann, L. Juha, M. Jurek, F. Y. Khattak, A. R. Khorsand, D. Klinger, M. Kozlova, T. Laarmann, H. J. Lee, R. W. Lee, K.-H. Meiwes-Broer, P. Mercere, W. J. Murphy, A. Przystawik, R. Redmer, H. Reinholz, D. Riley, G. Röpke, F. Rosmej, K. Saksl, R. Schott, R. Thiele, J. Tiggesbäumker, S. Toleikis, T. Tschentscher, I. Uschmann, H. J. Vollmer, J. S. Wark, *Nature Physics* **2009**, *5*, 693–696.

[3] H. Yoneda, Y. Inubushi, M. Yabashi, T. Katayama, T. Ishikawa, H. Ohashi, H. Yumoto, K. Yamauchi, H. Mimura, H. Kitamura, *Nature Communications* **2014**, *5*, 5080.

[4] H. Yoneda, Y. Inubushi, T. Tanaka, Y. Yamaguchi, F. Sato, S. Morimoto, T. Kumagai, M. Nagasono, A. Higashiya, M. Yabashi, T. Ishikawa, H. Ohashi, H. Kimura, H. Kitamura, R. Kodama, *Optics Express* **2009**, *17*, 23443.

[5] B. I. Cho, M. S. Cho, M. Kim, H.-K. Chung, B. Barbrel, K. Engelhorn, T. Burian, J. Chalupský, O. Ciricosta, G. L. Dakovski, V. Hájková, M. Holmes, L. Juha, J. Krzywinski, R. W. Lee, C. H. Nam, D. S. Rackstraw, S. Toleikis, J. J. Turner, S. M. Vinko, J. S. Wark, U. Zastrau, P. A. Heimann, *Physical Review Letters* **2017**, *119*, 075002.

[6] R. K. Lam, S. L. Raj, T. A. Pascal, C. Pemmaraju, L. Foglia, A. Simoncig, N. Fabris, P. Miotti, C. J. Hull, A. M. Rizzuto, J. W. Smith, R. Mincigrucci, C. Masciovecchio, A. Gessini, G. De Ninno, B. Diviacco, E. Roussel, S. Spampinati, G. Penco, S. Di Mitri, M. Trovò, M. B. Danailov, S. T. Christensen, D. Sokaras, T.-C. Weng, M. Coreno, L. Poletto, W. S. Drisdell, D. Prendergast, L. Giannessi, E. Principi, D. Nordlund, R. J. Saykally, C. P. Schwartz, *Chemical Physics Letters* **2018**, *703*, 112–116.

[7] A. Thomposn, D. Attwood, E. Gullikson, M. Howells, K. Kim, J. Kirz, J. Kortright, I. Lindau, Y. Liu, P. Pianetta, A. Robinson, J. Scofield, J. Underwood, G. Williams, H. Winick, *X-Ray Data Booklet*, third edition, Berkeley, **2009**.

[8] D. D. L. Chung, *Journal of Materials Science* **2002**, *37*, 1475–1489.

[9] A. Hirsch, *Nature Materials* **2010**, *9*, 868–871.

[10] H. W. Kroto, J. R. Heath, S. C. O'Brien, R. F. Curl, R. E. Smalley, *Nature* **1985**, *318*, 162–163.

[11] S. Iijima, T. Ichihashi, *Nature* **1993**, *363*, 603–605.

[12] K. S. Novoselov, *Science* **2004**, *306*, 666–669.

[13] P. Avouris, F. Xia, *MRS Bulletin* **2012**, *37*, 1225–1234.

[14] H. He, L. A. Pham-Huy, P. Dramou, D. Xiao, P. Zuo, C. Pham-Huy, *BioMed Research International* **2013**, *2013*, 1–12.

[15] G. Zhao, H. F. Mu, D. H. Wang, C. L. Yang, J. K. Wang, J. Y. Song, Z. C. Shao, *Physica Scripta* **2013**, *88*, 045601.

[16] J. S. Dickey, Jr., W. A. Bassett, J. M. Bird, M. S. Weathers, *Geology* **1983**, *11*, 219–220.

[17] D. H. Reitze, H. Ahn, M. C. Downer, *Physical Review B* **1992**, *45*, 2677–2693.

[18] A. Cavalleri, K. Sokolowski-Tinten, D. von der Linde, I. Spagnolatti, M. Bernasconi, G. Benedek, A. Podestà, P. Milani, *Europhysics Letters (EPL)* **2002**, *57*, 281–287.

[19] H. O. Jeschke, M. E. Garcia, K. H. Bennemann, *Physical Review Letters* **2001**, *87*, 015003.

[20] T. H. Maiman, *Physical Review Letters* **1960**, *4*, 564–566.

[21] J. Li, X. Ren, Y. Yin, K. Zhao, A. Chew, Y. Cheng, E. Cunningham, Y. Wang, S. Hu, Y. Wu, M. Chini, Z. Chang, *Nature Communications* **2017**, *8*, 186.

[22] C. Pellegrini, *The European Physical Journal H* **2012**, *37*, 659–708.

[23] C. Bocchetta, FERMI@Elettra - Conceptual Design Report, **2009**.

[24] *Springer Handbook of Lasers and Optics*, (Ed.: F. Träger), Springer, New York, **2007**.

[25] T. Tschentscher, C. Bressler, J. Grünert, A. Madsen, A. P. Mancuso, M. Meyer, A. Scherz, H. Sinn, U. Zastrau, *Applied Sciences* **2017**, *7*, 592.

[26] D. Attwood, A. Sakdinawat, *X-Rays and Extreme Ultraviolet Radiation: Principles and Applications*, 2nd ed., Cambridge University Press, Cambridge, **2016**.

[27] B. M. Kincaid, *Journal of Applied Physics* **1977**, *48*, 2684–2691.

[28] P. Emma, R. Akre, J. Arthur, R. Bionta, C. Bostedt, J. Bozek, A. Brachmann, P. Bucksbaum, R. Coffee, F.-J. Decker, Y. Ding, D. Dowell, S. Edstrom, A. Fisher, J. Frisch, S. Gilevich, J. Hastings, G. Hays, P. Hering, Z. Huang, R. Iverson, H. Loos, M. Messerschmidt, A. Miahnahri, S. Moeller, H.-D. Nuhn, G. Pile, D. Ratner, J. Rzepiela, D. Schultz, T. Smith, P. Stefan, H. Tompkins, J. Turner, J. Welch, W. White, J. Wu, G. Yocky, J. Galayda, *Nature Photonics* **2010**, *4*, 641–647.

[29] W. Ackermann, G. Asova, V. Ayvazyan, A. Azima, N. Baboi, J. Bähr, V. Balandin, B. Beutner, A. Brandt, A. Bolzmann, R. Brinkmann, O. I. Brovko, M. Castellano, P. Castro, L. Catani, E. Chiadroni, S. Choroba, A. Cianchi, J. T. Costello, D. Cubaynes, J. Dardis, W. Decking, H. Delsim-Hashemi, A. Delserieys, G. Di Pirro, M. Dohlus, S. Düsterer, A. Eckhardt, H. T. Edwards, B. Faatz, J. Feldhaus, K. Flöttmann, J. Frisch, L. Fröhlich, T. Garvey, U. Gensch, C. Gerth, M. Görler, N. Golubeva, H.-J. Grabosch, M. Grecki, O. Grimm, K. Hacker, U. Hahn, J. H. Han, K. Honkavaara, T. Hott, M. Hüning, Y. Ivanisenko, E. Jaeschke, W. Jalmuzna, T. Jezynski, R. Kammering, V. Katalev, K. Kavanagh, E. T. Kennedy, S. Khodyachykh, K. Klose, V. Kocharyan, M. Körfer, M. Kollewe, W. Koprek, S. Korepanov, D. Kostin, M. Krassilnikov, G. Kube, M. Kuhlmann, C. L. S. Lewis, L. Lilje, T. Limberg, D. Lipka, F. Löhl, H. Luna, M. Luong, M. Martins, M. Meyer, P. Michelato, V. Miltchev, W. D. Möller, L. Monaco, W. F. O. Müller, O. Napieralski, O. Napoly, P. Nicolosi, D. Nölle, T. Nuñez, A. Oppelt, C. Pagani, R. Paparella, N. Pchalek, J. Pedregosa-Gutierrez, B. Petersen, B. Petrosyan, G. Petrosyan, L. Petrosyan, J. Pflüger, E. Plönjes, L. Poletto, K. Pozniak, E. Prat, D. Proch, P. Pucyk, P. Radcliffe, H. Redlin, K. Rehlich, M. Richter, M. Roehrs, J. Roensch, R. Romaniuk, M. Ross, J. Rossbach, V. Rybnikov, M. Sachwitz, E. L. Saldin, W. Sandner, H. Schlarb, B. Schmidt, M. Schmitz, P. Schmüser, J. R. Schneider, E. A. Schneidmiller, S. Schnepp, S. Schreiber, M. Seidel, D. Sertore, A. V. Shabunov, C. Simon, S. Simrock, E. Sombrowski, A. A. Sorokin, P. Spanknebel, R. Spesyvtsev, L. Staykov, B. Steffen, F. Stephan, F. Stulle, H. Thom, K. Tiedtke, M. Tischer, S. Toleikis, R. Treusch, D. Trines, I. Tsakov, E. Vogel, T. Weiland, H. Weise, M. Wellhöfer, M. Wendt, I. Will, A. Winter, K. Wittenburg, W. Wurth, P. Yeates, M. V. Yurkov, I. Zagorodnov, K. Zapfe, *Nature Photonics* **2007**, *1*, 336–342.

[30] K. Tono, T. Togashi, Y. Inubushi, T. Sato, T. Katayama, K. Ogawa, H. Ohashi, H. Kimura, S. Takahashi, K. Takeshita, H. Tomizawa, S. Goto, T. Ishikawa, M. Yabashi, *New Journal of Physics* **2013**, *15*, 083035.

[31] E. Saldin, E. Schneidmiller, M. Yurkov, *Optics Communications* **1998**, *148*, 383–403.

[32] E. Allaria, R. Appio, L. Badano, W. Barletta, S. Bassanese, S. Biedron, A. Borga, E. Busetto, D. Castronovo, P. Cinquegrana, S. Cleva, D. Cocco, M. Cornacchia, P. Craievich, I. Cudin, G. D'Auria, M. Dal Forno, M. Danailov, R. De Monte, G. De Ninno, P. Delgiusto, A. Demidovich, S. Di Mitri, B. Diviacco, A. Fabris, R. Fabris, W. Fawley, M. Ferianis, E. Ferrari, S. Ferry, L. Froehlich, P. Furlan, G. Gaio, F. Gelmetti, L. Giannessi, M. Giannini, R. Gobessi, R. Ivanov, E. Karantzoulis, M. Lonza, A. Lutman, B. Mahieu, M. Milloch, S. Milton, M. Musardo, I. Nikolov, S. Noe, F. Parmigiani, G. Penco, M. Petronio, L. Pivetta, M. Predonzani, F. Rossi, L. Rumiz, A. Salom, C. Scafuri, C. Serpico, P. Sigalotti, S. Spampinati, C. Spezzani, M. Svandrlik, C. Svetina, S. Tazzari, M. Trovo, R. Umer, A. Vascotto, M. Veronese, R. Visintini, M. Zaccaria, D. Zangrando, M. Zangrando, *Nature Photonics* **2012**, *6*, 699–704.

[33] P. Rebernik Ribič, E. Roussel, G. Penn, G. De Ninno, L. Giannessi, G. Penco, E. Allaria, *Photonics* **2017**, *4*, 19.

[34] E. Allaria, C. Callegari, D. Cocco, W. M. Fawley, M. Kiskinova, C. Masciovecchio, F. Parmigiani, *New Journal of Physics* **2010**, *12*, 075002.

[35] L. Giannessi, E. Allaria, L. Badano, F. Bencivenga, C. Callegari, F. Capotondi, F. Cilento, P. Cinquegrana, M. Coreno, I. Cudin, G. D'Auria, M. Danailov, R. De Monte, G. De Ninno, P. Delgiusto, A. Demidovich, M. Di Fraia, S. Di Mitri, B. Diviacco, A. Fabris, R. Fabris, W. Fawley, M. Ferianis, P. Furlan Radivo, G. Gaio, D. Gauthier, F. Gelmetti, F. Iazzourene, S. Krecic, M. Lonza, N. Mahne, M. Malvestuto, C. Masciovecchio, M. Milloch, N. Mirian, F. Parmigiani, G. Penco, A. Perucchi, L. Pivetta, O. Plekan, M. Predonzani, E. Principi, L. Raimondi, P. Rebernik Ribič, F. Rossi, E. Roussel, L. Rumiz, C. Scafuri, C. Serpico, P. Sigalotti, S. Spampinati, C. Spezzani, M. Svandrlik, M. Trovò, A. Vascotto, M. Veronese, R. Visintini, D. Zangrando, M. Zangrando, *Proceedings of the 38th Int. Free Electron Laser Conf.* **2018**, *FEL2017*, in collab. with B. Kip (Ed.), C. Bruce (Ed.), S. RW (Ed.), Volker.

[36] R. W. Boyd, *Nonlinear Optics*, Academic Press, New York, **2008**.

[37] X.-C. Zhang, Y. Jin, K. Yang, L. J. Schowalter, *Physical Review Letters* **1992**, *69*, 2303–2306.

[38] Y. R. Shen, *The Principles of Nonlinear Optics*, Wiley & Sons Ltd, New York, **1984**.

[39] X. F. Li, A. L'Huillier, M. Ferray, L. A. Lompré, G. Mainfray, *Physical Review A* **1989**, *39*, 5751–5761.

[40] J. L. Krause, K. J. Schafer, K. C. Kulander, *Physical Review Letters* **1992**, *68*, 3535–3538.

[41] M. O. Krause, *Journal of Physical and Chemical Reference Data* **1979**, *8*, 307–327.

[42] Steudel Ralf, *Chemie Der Nichtmetalle, Synthesen - Strukturen - Bindung – Verwendung*, De Gruyter, Berlin, Boston, **2013**.

[43] Fitzer E., Kochling K.-H., Boehm H. P., Marsh H., *Pure and Applied Chemistry* **1995**, *67*, 473.

[44] X. Lu, H. Huang, N. Nemchuk, R. S. Ruoff, *Applied Physics Letters* **1999**, *75*, 193–195.

[45] J.-C. Charlier, J.-P. Michenaud, X. Gonze, J.-P. Vigneron, *Physical Review B* **1991**, *44*, 13237–13249.

[46] F. P. Bundy, W. A. Bassett, M. S. Weathers, R. J. Hemley, H. K. Mao, A. F. Goncharov, 13.

[47] J. Heremans, C. H. Olk, G. L. Eesley, J. Steinbeck, G. Dresselhaus, *Physical Review Letters* **1988**, *60*, 452–455.

[48] G. Galli, R. M. Martin, R. Car, M. Parrinello, *Physical Review Letters* **1989**, *63*, 988–991.

[49] G. Galli, R. M. Martin, R. Car, M. Parrinello, *Physical Review B* **1990**, *42*, 7470–7482.

[50] D. L. Beveridge, B. J. Bulkin, *Journal of Chemical Education* **1971**, *48*, 587.

[51] N. Ooi, A. Rairkar, J. B. Adams, *Carbon* **2006**, *44*, 231–242.

[52] R. Mincigrucci, E. Principi, F. Bencivenga, L. Foglia, A. Gessini, G. Kurdi, A. Simoncig, C. Masciovecchio, *Photonics* **2017**, *4*, 23.

[53] N. Tandon, J. Albrecht, L. Ram-Mohan, *Diamond and Related Materials* **2015**, *56*, 1–5.

[54] M. B. Danailov, F. Bencivenga, F. Capotondi, F. Casolari, P. Cinquegrana, A. Demidovich, E. Giangrisostomi, M. P. Kiskinova, G. Kurdi, M. Manfredda, C. Masciovecchio, R. Mincigrucci, I. P. Nikolov, E. Pedersoli, E. Principi, P. Sigalotti, *Optics Express* **2014**, *22*, 12869.

[55] *MATLAB*, version R2019a, Natick, Massachusetts: The MathWorks Inc, **2019**.

[56] R. K. Lam, S. L. Raj, T. A. Pascal, C. D. Pemmaraju, L. Foglia, A. Simoncig, N. Fabris, P. Miotti, C. J. Hull, A. M. Rizzuto, J. W. Smith, R. Mincigrucci, C. Masciovecchio, A. Gessini, E. Allaria, G. De Ninno, B. Diviacco, E. Roussel, S. Spampinati, G. Penco, S. Di Mitri, M. Trovò, M. Danailov, S. T. Christensen, D. Sokaras, T.-C. Weng, M. Coreno, L. Poletto, W. S. Drisdell, D. Prendergast, L. Giannessi, E. Principi, D. Nordlund, R. J. Saykally, C. P. Schwartz, *Physical Review Letters* **2018**, *120*, 023901.

[57] K. Wang, J. Wang, J. Fan, M. Lotya, A. O'Neill, D. Fox, Y. Feng, X. Zhang, B. Jiang, Q. Zhao, H. Zhang, J. N. Coleman, L. Zhang, W. J. Blau, *ACS Nano* **2013**, *7*, 9260–9267.

[58] K. Hatada, A. Di Cicco, *Journal of Electron Spectroscopy and Related Phenomena* **2014**, *196*, 177–180.

[59] R. Ahuja, P. A. Brühwiler, J. M. Wills, B. Johansson, N. Mårtensson, O. Eriksson, *Physical Review B* **1996**, *54*, 14396–14404.

[60] J. Hubbel, S. Seltzer, *Tables of X-Ray Mass Attenuation Coefficients and Mass Energy-Absorption Coefficients*, version 1.4, Gaithersburg, MD: National Institute of Standards and Technology, **2004**.

[61] T. Schoonjans, A. Brunetti, B. Golosio, M. Sanchez del Rio, V. A. Solé, C. Ferrero, L. Vincze, *Spectrochimica Acta Part B: Atomic Spectroscopy* **2011**, *66*, 776–784.

[62] S. Sharma, C. Ambrosch-Draxl, *Physica Scripta* **2004**, *T109*, 128.

[63] M. Schultze, K. Ramasesha, C. D. Pemmaraju, S. A. Sato, D. Whitmore, A. Gandman, J. S. Prell, L. J. Borja, D. Prendergast, K. Yabana, D. M. Neumark, S. R. Leone, *Science* **2014**, *346*, 1348–1352.

Acknowledgment

I would like to express my thanks to the people who enabled me to write this thesis. First of all I'd like to thank Michael Zürch for giving me the possibility to participate in his exciting research. To perform research at state of the art facilities abroad exceeded my expectations for a master thesis. All the help and advice are very much appreciated.
My thanks goes to Eckart Rühl who has agreed to be the supervisor of the master thesis. Martin Wolf is also thanked for being in the examination commission and welcoming me at Physical Chemistry department of the Fritz Haber Institute.
Further, I want to thank everyone from the FERMI beamtime including Craig Schwartz, Walter Drisdell, Michael Zürch, Shervin Fatehi, Sumana Raj, Hikaru Mizuno, and especially Tobias Helk, who also organized the beamtime in Paris. They made the beamtime enjoyable even when things didn't go as planned. Thanks goes to Emiliano Principi who helped me with the experimental specifications.
In the end I want to thank Stéphane Sebban and his colleagues at LOA whose efforts made the challenging experiment work that didn't make it into this thesis.

Eidesstattliche Erklärung

Lars	Hoffmann	4679422
Vorname	Name	Matrikelnummer

20.09.1993	Berlin	,
geboren am	geboren in	

an Eides statt, dass die vorliegende Arbeit von mir selbstständig und ohne unerlaubte Hilfe Dritter verfasst wurde und ich keine anderen als die angegebenen Quellen und Hilfsmittel verwendet sowie wörtliche und sinngemäße Zitate als solche kenntlich gemacht habe.

Diese Arbeit hat in gleicher oder ähnlicher Form noch keiner anderen Prüfungsbehörde vorgelegen und wurde bisher nicht veröffentlicht.

Ort, Datum	Unterschrift